HHS Public Access

Author manuscript

Chem Eng Sci. Author manuscript; available in PMC 2024 July 05.

Published in final edited form as:

Chem Eng Sci. 2024 March 05; 285: . doi:10.1016/j.ces.2023.119534.

*Corresponding Author: **Zoltan K. Nagy –** Davidson School of Chemical Engineering, Purdue University, 47907 West Lafayette, Indiana, United States; zknagy@purdue.edu.

Inyoung Hur – Davidson School of Chemical Engineering, Purdue University, 47907 West Lafayette, Indiana, United States;

Daniel Casas-Orozco – Davidson School of Chemical Engineering, Purdue University, 47907 West Lafayette, Indiana, United States;

Daniel Laky – Davidson School of Chemical Engineering, Purdue University, 47907 West Lafayette, Indiana, United States;

Francesco Destro – Davidson School of Chemical Engineering, Purdue University, 47907 West Lafayette, Indiana, United States; Department of Chemical Engineering, Massachusetts Institute of Technology, Cambridge, MA 02139

Credit Roles

Inyoung Hur: Conceptualization, Methodology, Software, Formal analysis, Investigation, Writing – Original Draft, Writing – Review and Editing, Visualization. **Daniel Casas-Orozco:** Conceptualization, Methodology, Software, Writing – Review and Editing. **Daniel Laky:** Writing – Review and Editing. **Francesco Destro:** Conceptualization, Writing – Review and Editing, Supervision. **Zoltan K. Nagy:** Conceptualization, Methodology, Writing – Review and Editing, Supervision, Project administration, Funding acquisition.

Nomenclature

Notations	Measure	Unit
$f(L,t)$	Crystal number distribution	$[\#\ m^{-3}\,\mu m^{-1}]$
$\dot{F}_k$	Flow rate on unit/stream k	$[m^3 s^{-1}]$
C	Concentration in solution	$[kg\,m^3]$
k_p	Primary nucleation rate coefficient	$[\#\ m^{-3}\,s^{-1}]$
p	Primary nucleation rate exponent	[-]
A_c	Exposed crystal surface	$[m^2]$
k_s	Secondary nucleation rate coefficient	$[\#\ m^{-3}\,s^{-1}]$
s	Secondary nucleation exponent	[-]
k_g	Growth rate coefficient, , and the activation energy of growth	$[m\,s^{-1}]$
g	Growth rate exponent	[-]
E_A	Activation energy of growth	$[J\,mol^{-1}]$
R_{cake}	Cake resistance	$[m^{-1}]$
R_{medium}	Filter mesh resistance	$[m^{-1}]$
V_{filt}	Filtrate volume	$[m^3]$
m_{filt}	Filtrate mass	$[kg]$
α_{cake}	Specific cake resistance	$[m\,kg^{-1}]$
μ_l	Viscosity of liquid	$[kg\,m^{-1}\,s^{-1}]$
μ_g	Viscosity of gas	$[kg\,m^{-1}\,s^{-1}]$
A_{filt}	Filter cake cross sectional area	$[m^2]$
ΔP	Pressure difference	$[Pa]$
ε	Porosity	[-]
ρ_s	Density of solid phase	[kg m^{-3}]
k_v	Volume factor of crystallizer	[-]

Digital design of an integrated purification system for continuous pharmaceutical manufacturing

Inyoung Hur[a], **Daniel Casas-Orozco**[a], **Daniel Laky**[a], **Francesco Destro**[a,b], **Zoltan K. Nagy**[a,*]

[a]Davidson School of Chemical Engineering, Purdue University, West Lafayette, IN 4797 USA.

Notations	Measure	Unit
$D_{j,ax}$	Pure component diffusivity	$\left[m^2 s^{-1}\right]$
v_l	Volume fluxes per unit area	$[m\,s^{-1}]$
k_{av}	Cake permeability	$[m^2]$
k_{rl}	Relative liquid permeability	[-]
k_{rg}	Relative gas permeability	[-]
W	Washing ratio	[-]
L_{cake}	Cake height	$[m]$
λ	Adsorption coefficient	[-]
d_i	Size	$[m]$
P_b	Minimum pressure threshold	$[Pa]$
S_∞	Equilibrium saturation of the cake	[-]
$m_{j,cake}$	Mass of component *i* in liquid per unit volume of the cake	$\left[kg\,m^{-3}\right]$
x_i	Mass fraction in liquid phase	[-]
$\dot{m}_j^{\mathrm{L}\rightarrow\mathrm{G}}$	Drying rate	$[kg\,m^{-3}s^{-1}]$
$h_{\mathrm{M,j}}$	Mass transfer parameter	$[kg\,m^{-1}s^{-1}]$
a_{V}	Specific surface area	$\left[m^{-1}\right]$
$\overline{c}_p$	Averaged heat capacity	$\left[J\,K^{-1}mol^{-1}\right]$
h_{T}	Heat transfer coefficient	[W m^{-2} K^{-1}]
λ_{latent}	Latent heat of vaporization	$\left[J\,kg^{-1}\right]$
$\dot{F}_{\mathrm{CR02}}^{out}$	outlet volumetric flow rate	$[m^3 s^{-1}]$
β_{CR01}	Fractional temperature drop	[-]
τ	Residence time	[s]
S_r	Reduced saturation	[-]
γ_j	Activity coefficient	[-]
η	Mass transfer limitation factor	[-]
P_{sat}	Saturation pressure	$[Pa]$
P_l	Liquid pressure	$[Pa]$
P_g	Gas pressure	$[Pa]$

[b]Department of Chemical Engineering, Massachusetts Institute of Technology, Cambridge, MA 02139

Abstract

In this work dynamic models of the continuous crystallization, filtration, deliquoring, washing, and drying steps are introduced, which are developed in the open-source pharmaceutical modeling tool PharmaPy. These models enable the simulation and digital design of an integrated continuous two-stage crystallization and filtration-drying carousel system. The carousel offers an intensified process that can manufacture products with tailored properties through optimal design and control. Results show that improved crystallization design enhances overall process efficiency by improving critical material attributes of the crystal slurry for downstream filtration and drying operations. The digital design of the integrated process achieves enhanced productivity while satisfying multiple design and product quality constraints. Additionally, the impact of model uncertainty on the optimal operating conditions is investigated. The findings demonstrate the systematic process development potential of PharmaPy, providing improved process understanding, design space identification, and optimized robust operation.

Keywords

Process Design & Development; Continuous Drug Purification; Process Intensification; Dynamic Flowsheet Simulation

1. Introduction

The convergence of Industry 4.0, process intensification (PI), and continuous manufacturing (CM) represents a transformative shift in the way pharmaceutical industries operate. PI optimizes production methods for efficiency and quality, while continuous manufacturing emphasizes the uninterrupted flow of products. Together, these concepts are reshaping traditional manufacturing paradigms, offering opportunities for cost reduction, quality improvement, and flexibility. This synergy is particularly crucial in the pharmaceutical sector, where precise and efficient production is vital for delivering targeted medications to patients while meeting rigorous regulatory standards. (Plumb et al., 2005; Jolliffe et al., 2017; Schaber et al., 2011).

One of the main challenges in developing integrated CM processes is optimizing the material flow while considering the thermodynamic and kinetic interplay between consecutive unit operations. To address potential issues in CM, various frameworks have been introduced, including quality-by-design (QbD), process analytical technology (PAT), and quality-by-control (QbC). These frameworks are supported by guidance documents from the United States Food & Drug Administration (FDA) and the International Council for Harmonization (ICH) which aim to promote the benefits of CM by defining a multidimensional operating region called the design space (DS) (ICH Q8, Q9, Q10). The DS is defined as a multidimensional operating region within the critical material attributes (CMAs) and critical process parameters (CPPs) space, which results in desirable critical quality attributes (CQAs) (ICH Q8). Simulation studies using digital twins have proven to

be a cost-effective alternative for optimizing CPPs without the need for expensive API or extensive experimental efforts (Jung et al., 2004; Stephanopoulos and Reklaitis, 2011).

Continuous drug purification poses a significant challenge in achieving end-to-end CM. Scaling up processes involving crystal slurry purification and isolation, which encompass crystallization, filtration, washing, and drying, is complex due to the interplay between these steps and their impact on multiple CQAs of the final product (Price et al., 2020; Simon et al., 2019). The influence of crystal properties, such as crystal size distribution (CSD) and shape, on filtration efficiency and moisture content of the final product has been extensively studied (Reynolds et al., 2003; Ottoboni et al., 2019; Ouchlyama and Tanaka, 1986).

Literature reports successful integration of continuous filtration systems with continuous crystallization, including sequential batch filtration with continuous drying units and the integration of continuous filtration carousel (CFC) with mixed-suspension-mixed-product-removal (MSMPR) crystallizers (Capellades et al., 2020; Ottoboni et al., 2019; Price et al., 2020; Acevedo et al., 2016; Domokos et al., 2020; Liu et al., 2019a). These studies investigate the impact of crystal properties (e.g., crystal size distribution, aspect ratio) on the moisture content and other CQAs (e.g., impurity content, size, etc.) of the filtered product. Similar investigations have been conducted with continuous slug flow crystallizers combined with continuous vacuum screw filters (Steenweg et al., 2021; Habicht and Wohlgemuth, 2022).

Despite these advancements, the design and performance of continuous filtration and drying processes in drug purification still heavily rely on empirical methodologies with loosely defined operations, lacking detailed evaluation of filtration efficiency and operating conditions (Simon et al., 2019; Wood et al., 2019). Ward *et al.* developed an analytical method for continuous crystallization followed by a continuous rotary drum filter with material recycle, and showed that the derived design equation with reduced-order model can predict the steady-state process behavior under nominal operating conditions of the integrated system (Ward et al., 2011). Sen *et al.* (2013) further utilized a flowsheet model to optimize process start-up for cooling crystallization, including one process decision variable per unit operation and the developed model is further integrated with an optimization-based control strategy (Sen *et al.*, 2014). The application of flowsheet simulation to an integrated process, including reaction, MSMPR, filtration and dissolution steps, where the critical material properties for filtration are calculated from the steady-state crystallization model output, was also demonstrated, indicating the importance of optimization of the overall flowsheet, versus the individual unit operations, to achieve optimal performance of the integrated system (Nagy et al., 2020; Nagy et al., 2021). However, the model addressed in the flowsheet does not simulate the detailed operating steps for the filtration, such as deliquoring, washing, and drying, and there is no investigation of the effect of parametric uncertainties of the optimized control variables. Digital twins constructed using mechanistic models enable uncertainty and sensitivity analyses for optimization and design space identification, i.e., using Monte-Carlo simulations (Destro et al., 2022a; Destro et al., 2022b; García-Muñoz et al., 2018). Recent studies have ranked the effect of CPPs on CQAs and highlighted the need for quantitative analysis of the feasible operating window to mitigate disturbances and uncertainties in process design and operation (Maloney et al., 2020).

However integrated drug purification studies have mainly focused on experimental process developments and lack the application of simultaneous model-based design to address the influence of crystallization conditions on filtration and drying efficiency in both batch and continuous operation modes (Destro et al., 2021; Boukouvala et al., 2012, Boukouvala et al., 2013, Öner et al., 2020; Yang et al., 2017). Despite the pronounced interconnectivity in continuous integrated processes, and the proven benefits of flowsheet modeling approaches to enable the detailed analysis and digital design of the overall process, the application of the digital design frameworks to continuous purification processes is yet to be explored.

This study presents a model-based design approach for an integrated continuous purification flowsheet that connects the crystallization, filtration, washing, and drying steps. A detailed digital representation of an intensified processing platform was developed using mechanistic models for each step of the drug purification process on the PharmaPy platform (Casas-Orozco et al., 2021). Dynamic simulation is implemented on the platform, facilitating the identification of key model parameters and their impact on CQAs. Since detailed quantification of the parametric uncertainties are included together with the digital model, this allows the characterization of the reliability of model predictions, therefore the model can be considered as a *static digital twin* (SDT). This follows the extended definition of digital twins, according to which a mathematical model together with its quantified prediction uncertainty domain, can be considered as a digital twin (virtual representation of the real process). In this context a digital twin can be *dynamic* (DDT), when there is a two-way automated data exchange between the physical (real process) and virtual (model) systems *with quantification of prediction uncertainties*, or can be *static* (SDT), when there is no real-time data exchange, but the model is combined with full quantification of prediction uncertainties. The optimal process operating conditions were determined using a constrained simulation-optimization framework, enforcing target process yield and CQAs for the integrated system. Sensitivity analysis was performed to assess the robustness of the optimal performance by considering uncertainties in model parameters and their impact on CQAs and process throughput.

The remainder of this manuscript is organized as follows. The integrated drug purification flowsheet is first described in Section 2, together with the mathematical models used to describe the process. The optimization formulation is explained in Section 3, with in silico investigations and design space analysis for the integrated flowsheet model presented in Section 4, Section 5 summarizes the final conclusions.

2. Problem statement

2.1 Process description: Flowsheet model for the integrated drug purification system

The API purification process shown in Figure 1 consists of a 2-step cooling crystallization followed by an intensified continuous filtration carousel (CFC) unit. Two MSMPR cooling crystallizers are operated in series to obtain a slurry stream. A saturated, crystal-free solution at inlet temperature (T_{feed}) is continuously introduced into the first crystallizer (CR01), triggering nucleation at a rate decided by the residence time of CR01 (τ_{CR01}). The resulting slurry is then continuously transferred to CR02. The slurry from CR02 is processed in a carousel filter-dryer with 5 vertical cylinder ports anchored around a central axis, where the

cake undergoes one or more steps among filtration, washing, and drying steps driven by the pressure gradient. After each filtration (t_{filt}) and drying cycle time (t_{drying}), the port rotates to the next station, enabling sequential batch downstream purification of the continuous upstream slurry.

Filtration and deliquoring are performed in F01, where the slurry from CR02 is intermittently fed and the filtrate is collected at a filtrate receiver. The wet cake then proceeds to deliquoring in DL01, where a pressure drop (ΔP) is applied to remove the liquid loosely contained in the cake. The deliquored cake undergoes displacement washing in W01 using ethanol as a washing solvent calibrated by the imposed washing ratio (W), followed by secondary deliquoring in DL02. The washing step reduces impurities and remaining API concentration, minimizing changes to the CSD during subsequent isolation and aiding cake drying by using a more volatile solvent. The remaining mother liquor is withdrawn by introducing hot air at the set temperature (T_{drying}) during drying at DR01, assuming only mass transfer occurs. The final dried API powder is ejected using a mechanical piston. The uncertainty of the mesh resistance from the fouling disturbances is neglected for the purpose of the simulation studies.

To integrate the continuous crystallization section with the batch operation of the CFC, the CFC platform is incorporated into a sub-flowsheet PharmaPy simulation object. This object coordinates the execution of the crystallizer and CFC models, configuration of processing steps, and material transfer. Intermediate slurry property values from CR02 are extracted at increments equal to the carousel cycle time ($t_{cycle} = t_{filt} + t_{dry}$) and used as inputs in calculating necessary cake properties and CMAs during the dynamic batch operation in the carousel as shown in Figure 2 (Appendix B). This integration enables a seamless connection between the continuous crystallization section and the batch operation of the CFC unit. For more detailed descriptions of the CFC setup in conjunction with crystallization, the readers are encouraged to refer to Domokos et al., (2020) and Destro et al., (2021).

2.2 Mathematical modeling of the continuous purification process

The following section describes the dynamic mathematical models of the individual unit operations used in this work. The crystallizer model is introduced first and followed by the solid-liquid-separation model, which covers filtration-deliquoring, washing, and drying steps.

2.2.1 Continuous crystallization—

A continuous MSMPR crystallizer was modeled using a one-dimensional population balance model (PBM) to describe the behavior of the solid phase. A general population balance model has been developed, including primary nucleation, secondary nucleation, size-independent growth, and size-independent dissolution kinetic mechanisms (Randolph et al., 1971; Szilagyi et al., 2020), with relative supersaturation (σ) as the main driving force for crystal formation. The PBM assuming homogeneous mixing is formulated in Eq. (1). The equation solves for the temporal evolution of number-based crystal density function.

$$\frac{\partial(f(L,t)_i V_i)}{\partial t} + V_i \cdot \frac{\partial(Gf(L,t)_i)}{\partial L} = V_i(B_p + B_s)\delta_{L,\,L_0} + \sum_k \dot{F}_k f(L,t)_k,$$
$$k \in \{1, .., N_{stream}\},\ \forall i \in \{CR_{01}, CR_{02}\},\ \sigma > 0 \tag{1}$$

Here, $f(L,t)_i$ is the crystal number distribution in a unit volume of slurry of i^{th} crystallizer at crystal size coordinate L at time t. V_i is the volume of the slurry in i^{th} crystallizer, $\dot{F}_k$ is the flow rate of the feed k coming in or out of the system (positive for input and negative for output flows), $f(L,t)_k$ is the crystal number distribution in a unit volume of slurry of the feed k, L_0 is the nuclei size, and δ is the Kronecker delta of target API species which is further defined as:

$$\delta_{L,\,L_0} = \begin{cases} 1, & L = L_0 \\ 0, & L \neq L_0 \end{cases} \tag{2}$$

Kinetics terms in Eq. (1) are growth rate, G, primary and secondary nucleation rate, B_p and B_s, respectively. All these kinetic mechanisms are driven by relative supersaturation, σ,

$$\sigma = \frac{C - C_s}{C_s} \tag{3}$$

where C is the liquid solute concentration and C_s is the equilibrium solubility calculated by the modified Apelblat equation given by:

$$C_s = \exp\left[a_1 + \frac{a_2}{T} + a_3 \ln(T)\right] \tag{4}$$

where a_1, a_2, and a_3 are constants found by nonlinear regression of solubility data. The primary nucleation rate B_p is described by the power law of relative supersaturation:

$$B_p = k_p \sigma^p \tag{5}$$

where k_p and p denote the primary nucleation rate coefficient and the primary nucleation rate exponent, respectively. The secondary nucleation B_s is expressed as the function of the specific surface area of crystals and the relative supersaturation:

$$B_s = k_s \sigma^s A_c \tag{6}$$

$$A_c = k_A \int_0^\infty L^2 f(L,t) dL \tag{7}$$

where k_s and s denote the secondary nucleation rate coefficient and the secondary nucleation rate exponent, respectively. k_A is the surface shape factor, and A_c is exposed crystal surface within the system. The growth rate is assumed to be supersaturation and temperature-dependent.

$$G = k_g \sigma^g \exp\left[-\frac{E_A}{RT}\right] \tag{8}$$

where k_g, g and E_A denote the growth rate coefficient, growth rate exponent, and the activation energy of growth, respectively. T is temperature in Kelvin, and R is the ideal gas constant. The equation system is closed with the mass balance on liquid phase.

$$\frac{\partial(\epsilon C_j V_i)}{\partial t} = -3V_i k_v \rho_{cry} \delta_{j,\,target} \int_0^\infty G(L,T) L^2 f(L,t)_i dL + \sum_k \dot{F}_k \epsilon_k C_{k,j},\ \sigma > 0$$
$$\forall i \in \{CR_{01}, CR_{02}\},\ \forall j \in \{1, \ldots, N_{comp}\},\ k \in \{1, .., N_{stream}\} \tag{9}$$

$$\epsilon = 1 - k_v \int_0^\infty L^3 f(L,t) dL \tag{10}$$

where ρ_{cry} the density of crystals, k_v is the volumetric shape factor of the target API compound crystals and ϵ is the volumetric fraction of the liquid in the slurry phase, following the definition in Eq. (10), C_j is a concentration of component j in the liquid phase, $\delta_{j,\,target}$ is a Kronecker delta of target API species (Eq. 5), $C_{k,j}$ is a concentration of component j in the feed k. A semi-discretized version using high-resolution finite volume method (HR-FVM) applied to the PBM (Eq. 1) is used to simulate the crystallization system (Leveque et al., 2002; Casas-Orozco et al., 2021; Gunawan et al., 2004). Boundary and initial conditions on f are given by:

$$\begin{cases} f(0,t) = \dfrac{B_p + B_s}{G} \\ f(L,0) = f_0 \end{cases} \tag{11}$$

where f_0 denotes the initial crystallization size distribution which is 0 for non-seeded process and distribution of seed material for seeded process.

2.2.2 Solid-liquid separation model—The following section presents the solid-liquid separation models from filtration, deliquoring, washing, and drying step. The consisting material and energy balance models utilize averaged cake properties ($\bar{pr}$) to simulate the physical phenomenon occurring inside the cake, *viz.*, porosity of the cake (ε), cake resistivity (α), irreducible saturation (S_∞), threshold pressure (P_b), and permeability of the cake (k_{av}) from full CSD, which is one of the parameters on which filterability of the slurry is highly dependent (Nagy et al., 2020). The calculation of the cake properties has been explained in the Appendix B.

Filtration model: A Nutsche filtration model is used to describe F01. The process of dead-end filtration is described by Darcy's Law (Muskat and Meres, 1936), which gives the superficial velocity of the filtrate through a porous medium. The driving force for filtration is the pressure gradient across the filter (ΔP), which is equal to, or higher than the threshold pressure (P_b). This includes the contributions of the wet cake (ΔP_{cake}) and that of the filter medium (ΔP_{filter}) (Eq. (12):

$$\Delta P = \Delta P_{cake} + \Delta P_{filter} \tag{12}$$

$$Q(t) = \frac{dV_{filt}}{dt} = \frac{\Delta P A_{filt}}{\mu_l (R_{cake} + R_{medium})} \tag{13}$$

$$\frac{dm_{filt}}{dt} = \frac{\Delta P}{\mu_l \left(\frac{\alpha_{cake} C_{filt} m_{filt}}{A_{filt}^2 \rho_l^2} + \frac{R_{medium}}{A_{filt} \rho_l} \right)} \tag{14}$$

$$\frac{dm_{hold}}{dt} = -\frac{dm_{filt}}{dt} \tag{15}$$

The instantaneous filtrate flowrate under constant pressure is expanded by flow resistances R_{cake} and R_{medium} in Eq. (13), and the full filtration model has been given in Eq. (14), where V_{filt} is the volume of filtrate, m_{filt} is the mass of filtrate, m_{hold} is the mass of mother liquor in the wet cake, μ_l is the liquid phase viscosity, ρ_l is the density of the liquid, α_{cake} is the specific cake resistance, C_{filt} is solid concentration, and A_{filt} is the cross-sectional area of the filter mesh. The filter cake is considered to be resistant to compression because of the rapid settling speed of the solids to form a thin cake in the small-scale filtration process.

The mass of material in the filtrate receiver is calculated by the mass of filtrate in Eq. (15). The variable C_{filt} is the solid mass per volume of filtrate, which is assumed to be constant throughout the filtration process (Eq. (16)).

$$C_{filt} = \frac{V_{slurry} C_{slurry}}{V_{filt,\,final}} \tag{16}$$

$$V_{filt,\,final} = V_{slurry}\left[1 - \frac{C_{slurry}}{\rho_s}\left(\frac{\varepsilon}{1-\varepsilon}\right)\right] \tag{17}$$

where ε is the porosity of the cake, and $V_{filt,\,final}$ is the volume of filtrate at the end of filtration, V_{slurry} is the volume of slurry for the filtration, and ρ_s is density of solid. The solid concentration of the slurry (C_{slurry}) is given by:

$$C_{slurry} = k_v \mu_3 \rho_s \tag{18}$$

$$\mu_3 = \int_0^\infty L^3 f(L,t)\,dL \tag{19}$$

Here, k_v is the volume shape factor of the crystal and μ_3 is third moment calculated by the outlet CSD from the crystallizer. After Eq. (14) is solved, the mass of dry (m_{dry}) and wet cake (m_{wet}) can be calculated as:

$$m_{dry}(t) = \frac{C_{slurry} m_{filt}(t)}{\rho_l} \tag{20}$$

$$m_{wet}(t) = m_{dry}(t)\left[1 + \frac{\rho_l}{\rho_s}\left(\frac{\varepsilon}{1-\varepsilon}\right)\right] \tag{21}$$

Washing model: The 1-D isothermal advection-diffusion equation is commonly used to describe the washing process (Ottoboni et al., 2022; Destro et al., 2021). In this work, the equation is generalized for both saturated and deliquored cakes, and it includes the linear sorption effects of adsorbates to solution concentration as a term in the mass balance on the liquid phase (Eriksson et al., 1996). The assumptions made are that the washing solvent

evenly penetrates the cake surface without causing cracking or shrinkage, and it does not create any preferential paths. The mass balance on the liquid phase (Eq. (22)) with uniform porosity for cakes (Lapidus and Amundson, 1952) is written:

$$\frac{\partial C_j}{\partial t} + u_l \frac{\partial C_j}{\partial z} - \frac{\partial}{\partial z}\left(D_{j,ax}\frac{\partial C_j}{\partial z}\right) = -\frac{1-\varepsilon}{\varepsilon}\frac{\partial (K \cdot C_j)}{\partial t}, \ \forall j \in \{1, \ldots, N_{comp}\} \tag{22}$$

$$C_j(t,0) = C_{j,wash} \ \ when\, z = 0,\, t > 0 \tag{23}$$

$$C_j(0,z) = C_j(z) \ \ \ when\, t = 0,\, z > 0 \tag{24}$$

where C_j is concentration species j in liquid phase, $C_{j,wash}$ is concentration of species j in washing solvent, K is adsorption coefficient and $D_{j,ax}$ is the pure component diffusivity of a species j. The advection velocity (u_l) of the liquid and gas phase is expanded from superficial velocity (v_l) calculated by Darcy's equation (Muskat and Meres, 1936):

$$u_l = \frac{v_l}{\varepsilon S} = -\frac{k_{av} k_{rl}}{\mu_l \varepsilon S}\frac{dP_l}{dz} \tag{25}$$

where v_l is the volume fluxes per unit area of the medium of liquid phase, μ_l is the viscosities of the liquid phase, S is the ratio between the volume of the liquid uptake and the volume of pores of the cake, P_l is pressure of liquid phase, k_{av} is the cake's permeability, and k_{rl} is the relative liquid permeability, which can be calculated by the empirical relations presented in Wakeman *et al* (Wakeman, 1979). The dynamic axial, liquid-phase concentration profiles of solvents and impurities is calculated through the analytical solution of Eq.(22) (Eriksson et al., 1996, Destro et al., 2021).

$$C_j^*(t,z) = \frac{C_j(t,\ z) - C_{j,wash}}{C_j(0,\ z) - C_{j,wash}} = 1 - \frac{1}{2}\left[\mathrm{erfc}\left(z\sqrt{\frac{1}{4\lambda D_{j,ax} t}} - u_l\sqrt{\frac{\lambda t}{4D_{j,ax}}}\right) - \exp\left(\frac{u_l z}{D_{j,ax}}\right)\mathrm{erfc}\left(z\sqrt{\frac{1}{4\lambda D_{j,ax} t}} + u_l\sqrt{\frac{\lambda t}{4D_{j,ax}}}\right)\right] \tag{26}$$

Washing ratio $W = \left(\frac{Volume\,of\,wash\,solvent\,used}{Volume\,of\,liquid\,in\,the\,pores}\right)$ was used to characterize the time in the washing step operation, which allows to determine total washing time as $t_{wash} = \frac{W A_{filt}\int_0^{L_{cake}} \varepsilon \,\mathrm{S}\,\mathrm{dz}}{u_l}$. Component adsorption coefficient λ is defined as follows (Eriksson et al., 1996):

$$\lambda = \frac{1}{1 - K + \frac{K}{\varepsilon}} \tag{27}$$

which is set to 1 by assuming equilibrium coefficient $K = 0$.

The effective dispersion coefficient, axial diffusivity $D_{j,ax}$, accounting for pores in the particles in the filter cake has been calculated from the diffusivity of pure component j (Wakeman and Tarleton, 2007) (Appendix B). At the end of washing, the average concentration inside the cake $(\overline{C_j})$ is calculated.

$$\overline{C_j} = \frac{C_j(t=0,\, z) - C_{j,\, wash}}{L_{cake}} \int_0^{L_{cake}} C_j^*(t = t_{wash},\, z)dz + C_{j,\, wash} \tag{28}$$

Deliquoring model: The governing equations for the dynamic pressure or vacuum deliquoring model are written as a material balance with a liquid axial advection velocity (u_l). The equation is solved for the overall liquid composition of the cake during the deliquoring process (Destro et al., 2021).

$$\frac{\partial(\varepsilon S)}{\partial t} = -\frac{\partial u_l}{\partial z} \tag{29}$$

The initial and boundary conditions for the model are:

$$\begin{aligned} S(t=0, z) &= 1, \ \forall z > 0 \\ S(t, z=0) &= 0, \ \forall t > 0 \end{aligned} \tag{30}$$

A component material balance in the liquid phase reads:

$$\frac{\partial C_j}{\partial t} = -\frac{u_l}{S}\frac{\partial C_j}{\partial z}, \ j = 1, \ldots N_{comp} \tag{31}$$

The initial condition is the initial composition of liquid phase (C_j^{init}) of the cake, and boundary condition represents the physical phenomenon where there is no flux of component j on the top of the cake:

$$\frac{\partial C_j}{\partial z}(t, z = 0 -) = 0, \ \forall t > 0$$
$$C_j(t = 0, z) = C_j^{init}, \ \forall z > 0 \tag{32}$$

The Eq. (29) and Eq. (31) are rearranged in dimensionless form to increase the numerical stability regardless of the size of the cake to be deliquored in the simulation. The readers are encouraged to refer to Appendix C for the detailed non-dimensional reformulation of the model and numerical solution scheme.

In the interest to quantify the relative mass composition of species of interest in the cake as a CQA of the process, the following formulation has been used along with the material balance.

$$m_{j,\,cake}(t,\,z) = \varepsilon S(t,\,z) C_j(t,\,z), \ \forall j \in \{1,\,\ldots,\,N_{comp}\} \tag{33}$$

$m_{j,\,cake}$ is the mass of component j in liquid per unit volume of the cake.

2.2.3 Drying model—In recent years, there has been increasing interest in improving models for predicting drying of multi-phase system (Levi-Hevroni et al., 2007, Dodda et al., 2015). This study builds upon existing literature (Destro et al., 2021) and presents a comprehensive representation of the system by considering both macroscopic transfer dynamics between phases and composition changes within a single phase. The global and component-wise material balances for the liquid phase inside the cake are depicted in Eq. (34) and Eq. (35):

$$\bar{\rho}_l \varepsilon \frac{\partial S}{\partial t} = -\sum_{j=1}^{n_{comp}} \dot{m}_j \, L \rightarrow G \tag{34}$$

$$\bar{\rho}_l \varepsilon S \frac{\partial x_j}{\partial t} = -\dot{m}_j \, L \rightarrow G - \bar{\rho}_l \varepsilon x_j \frac{\partial S}{\partial t}, \ \forall j \in \{1,\,\ldots,\,N_{comp}\} \tag{35}$$

where x_j is the mass fraction of species j in the liquid phase, and $\overline{\rho}_l$ is the average density of the liquid phase. Gas phase material balances accounting for the convective drying gas inlet are also needed to complete system description. The flow rate of the gas phase is written according to single-phase flow from Darcy's Law (Dullien, 1992).

$$u_g = \frac{v_g}{\varepsilon(1 - S)} = -\frac{k_{av} k_{rg}}{\mu_g} \frac{dP_g}{dz}$$

(36)

The component-wise mass balance for the gas phase reads:

$$\bar{\rho}_g \varepsilon (1-S)\frac{\partial y_j}{\partial t} = -u_g \bar{\rho}_g \frac{\partial y_j}{\partial z} + \dot{m}_j{}^{L\to G} - \frac{y_j \bar{\rho}_g}{\bar{\rho}_l}\sum_{j=1}^{n_{comp}} \dot{m}_j{}^{L\to G},\ \forall j \in \{1, \ldots, N_{comp}\}$$

(37)

where y_j is the mass fraction of species i in the gas phase, $\overline{\rho}_g$ is the average density of the gas phase, μ_g is the viscosity of the gas, and k_{rg} is the relative gas permeability. Pressure drop of the gas phase across the cake is assumed to be linear. Drying rate $\dot{m}_j{}^{L\to G}$ is computed as Chhabra and Shankar (2017):

$$\dot{m}_j{}^{L\to G} = \begin{cases} h_{M,j} a_V \left(y_j^* - y_j\right)\eta, & y_j^* > y_j \\ 0, & y_j^* < y_j \end{cases}, \forall i \in \{1, \ldots, N_{comp}\}$$

(38)

$$y_j^* = \gamma_j x_j \frac{P_{sat,\,j}(T_c)}{P}$$

(39)

$$\eta = f(S)$$

(40)

where $h_{M,j}$ and a_V is mass transfer coefficient for drying of a species j and specific surface area of crystals, $P_{sat,\,j}(T_c)$ is the saturation pressure of a species j at T_c (calculated with the Antoine equation), γ_j is an activity coefficient of a species j in the liquid phase. η is a mass transfer limitation factor to the drying rate that occurs when S is below a critical value as a drying experiment on paracetamol shows (Destro et al., 2021).

The energy balance considers temperature variations between phases to provide a more realistic description of simultaneous convective drying and evaporative drying. The solid and liquid phases are assumed to be in thermal equilibrium and are lumped under the condensed phase due to rapid heat exchange between them, as shown in Eq. (41)-(42).

$$\bar{\rho}_g \bar{c}_{v,g} \varepsilon (1-S)\frac{\partial T_g}{\partial t} = -u_g \bar{\rho}_g \bar{c}_{p,g}\frac{\partial T_g}{\partial z} - h_T a_V (T_g - T_c) + \sum_{j=1}^{n_{comp}} \dot{m}_j{}^{L\to G} \bar{c}_{p,g}(T_c - T_g)$$

(41)

$$(c_{p,s}(1-\varepsilon)\rho_s + \bar{c}_{p,l}\varepsilon S\bar{\rho}_l)\frac{\partial T_c}{\partial t} = -\sum_{j=1}^{n_{comp}} \dot{m}_j L \rightarrow G\lambda_{latent,j} + h_T a_V (T_g - T_c) \tag{42}$$

where T_g is temperature of the gas phase, T_c is temperature of the condensed phase, $\bar{c}_{p,g}$ and $\bar{c}_{v,g}$ is the averaged isobaric and isochoric specific heat capacity of the gas phase respecitively, $c_{p,s}$ is the isobaric specific heat capacity of the solids, $\bar{c}_{p,l}$ is the averaged isobaric specific heat capacity of liquid phase, h_T is the heat transfer coefficient, $\lambda_{latent,j}$ is the latent heat of vaporization of a species j. Heat transfer coefficient h_T has been set to 10 W/m^2K from running the drying step in an empty port of a lab-scale carousel in manual mode. Newton's cooling law in a parallel tublar flow exchanger between hot drying gas and ambient temperature is assumed. The initial condition of the mass balance of solid-gas phase is output calculated from the previous model or the user input. The inlet drying gas is assumed be pure nitrogen. The initial temperature is set to be same as room temperuatre (T_{room}). Hence, boundary conditions of the gas phase are set to be the composition and temperature of the drying medium (Eq. (43)-(44)).

$$\begin{cases} x_j(0,z) = from user input, & \forall z > 0 \\ y_j(0,z) = 0, & \forall z > 0 \\ T_c(0,z) = T_g(0,z) = T_{room}, & \forall z > 0 \end{cases} \tag{43}$$

$$\begin{cases} \dfrac{\partial y_j(t,0)}{\partial z} = 0, & \forall t > 0 \\ T_g(t,0) = T_{drying}, & \forall t > 0 \end{cases} \tag{44}$$

The resulting partial differential equation system (PDEs) is converted into an ODE system by semi-discretizing the axial coordinate using high-resolution finite volume method with 50 equally spaced increments. The resulting ODE system is solved with CVODEs packages from SUNDIALS suite (Hindmarsh et al., 2005).

3. Optimization of operational design and simulation case studies

3.1 Digital design by steady-state optimization

The constructed flowsheet consisting of the 2-step MSMPR and a CFC operation was simulated for paracetamol in 2-propanol as a case study. The known system-specific constants are listed in Table 1, and solubility constants were calculated by fitting the Eq. (4) to the solubility data (Granberg et al., 1999, Szilagyi et al., 2020).

The system dynamics to steady-state and production of dry product with consistent quality was examined under a set of fixed operating conditions. The simulated steady-state outputs

were obtained by setting the simulation time to 20 residence times for the crystallizers, which ensures the residual supersaturation in CR02 is exhausted and the crystallization reaches steady state. The feed temperature (T_{feed}) and CR02 cooling jacket temperature (T_{CR02}) are set based on the target yield, which is dictated by the solubility differences. Given the fixed volume of CR01, the residence time of CR01 (τ_{CR01}) determines the flowrate at which the slurry is introduced to CR02 ($\dot{F}_{CR01}$) (Eq. (45)), and the required volume of CR02 (V_{CR02}) can be computed based on the residence time of CR02 (τ_{CR02}) (Eq. (46))

$$\dot{F}_{CR01} = \frac{V_{CR01}}{\tau_{CR01}} \tag{45}$$

$$V_{CR02} = \dot{F}_{CR01}\tau_{CR02} \tag{46}$$

Among the available operating variables introduced, we specify T_{feed} and T_{CR02} to set an achievable target yield. Hence, the vector of free decision variables for the integrated crystallization and carousel process design is chosen to be $\boldsymbol{d} \equiv \{\beta_{CR01}, \tau_{CR01}, \tau_{CR02}, t_{filt}, t_{drying}, \Delta P, W, T_{drying}\}$, with the corresponding unit operations summarized in Table 2.

A steady-state optimization problem was formulated to maximize product throughput, as defined by Eq. (47), while maintaining target CQAs, *viz.* crystal size and residual cake moisture for the dried product, which are considered as process constraints, as shown in Eqs.(48)-(52):

$$\max_{d_p \in d} \left\{ Throughput = \frac{\dot{F}^{out}_{CR02}\tau_{CR02}C_{slurry}}{t_{filt} + t_{drying}} \right\} \tag{47}$$

$$s.t. \quad C_{sat}(T_{feed}) - C_{CR02}(T_{CR02}) > 0.9\,(C_{sat}(T_{feed}) - C_{sat}(T_{CR02})) \tag{48}$$

$$L_{crystal}\left(= \frac{\mu_1}{\mu_0} \right) > 50\,(\mu m) \tag{49}$$

$$S_{cake,\,dry} < 0.05\,(\mathrm{v/v}) \tag{50}$$

$$\dot{F}^{out}_{\mathrm{CR02}} t_{filt} < 10\,(ml) \tag{51}$$

$$d_{p,\,lb} < d_p < d_{p,\,ub}, \quad \forall d_p \in \boldsymbol{d} \tag{52}$$

where $C_{sat}(T)$ is the saturated concentration at the given temperature, T, obtained from the solubility curve, $C_{CR02}(T_{CR02})$ is the solution concentration of CR02 at T_{CR02}, $\dot{F}^{out}_{\mathrm{CR02}}$ is the outlet volumetric flow rate of CR02, and μ_n is n^{th} moment of the CSD, d_p is decision variable, $d_{p,lb}$ and $d_{p,ub}$ are lower and upper variable bounds. Fractional temperature drop, β_{CR01}, is calculated as shown in Eq. (53).

$$\beta_{CR01} = \frac{T_{CR01} - T_{CR02}}{T_{feed} - T_{CR02}} \tag{53}$$

Here, Eq.(47) indicates maximization of the dry product throughput subject to the aforementioned CQA constraints. For this case study, the following values are fixed at $T_{feed} = 40\,°\mathrm{C}$, $T_{CR02} = -10\,°\mathrm{C}$, and $V_{CR01} = 250\,\mathrm{mL}$. The first constraint (Eq.(48)) enforces practical crystallization yield to be at least 90% of the theoretical yield calculated from the solubility information at T_{feed} and T_{CR02}. Crystal mean size ($L_{crystal}$) has been targeted to be greater than 50 μm (Eq. (49)). These constraints ensure the direct design of crystal size of the product resulted from the crystallization, required for improving the filterability and overall manufacturability, since it is established that crystals with smaller particle size tend to agglomerate and have poorer flowability than the larger-sized crystals (Kaialy et al., 2012). Additionally, cake moisture after drying in DR01 ($S_{cake,\,dry}$) is imposed to be less than or equal to 0.05 (Eq. (50)). Lastly, Eq. (51) considers a maximum hold-up capacity of CFC port of 10 mL, whereas variable bounds described in Eq. (52) are shown in Table 2. The mathematical model and optimization problem were implemented in PharmaPy using a sequential simulation-optimization approach. The systematic workflow on digital design is presented on the following sections.

3.2 Two-step solution strategy of the digital design

To achieve multiple simultaneous design goals, a good understanding of the feasible design space is necessary before addressing the solution of the digital design problem by optimization. Among the set of operating variables and variable bounds introduced in Eq. (49), a grid-based design space identification procedure is employed with four operating variables [β_{CR01}, τ_{CR01}, τ_{CR02}, T_{drying}]. Different combinations of the possible critical process parameters (CPPs) have been utilized to carry out grid-based simulations on the continuous unit operations, starting from the standalone crystallization (Section 4.1.1) to the integrated crystallization-CFC system (Section 4.1.2). First, a grid over the CPPs is predefined for the

three crystallization operating variables, $[\beta_{CR01}, \tau_{CR01}, \tau_{CR02}]$, which identifies areas where slurry concentration can be maximized while producing a product quality corresponding to the target value. The grid is built with 9 evenly spaced points following the defined boundaries as below:

$$0 < \beta_{CR01} < 1 \tag{54}$$

$$20 < \tau_{CR01} < 120 \tag{55}$$

$$20 < \tau_{CR02} < 120 \tag{56}$$

The other CFC operating variable, T_{drying}, is also discretized for the integrated crystallization-CFC design space identification, based on following scheme:

$$30 < T_{drying} < 70 \tag{57}$$

For each point, a PharmaPy flowsheet is called by setting a framework at varying operating conditions and served as a tool to find the optimum operating strategy within the operating regime, while also revealing connections between operating variables and critical outputs (e.g. CMAs, CQAs, objective values, etc.). The flowsheet simulations can identify reasonable initial guesses for the optimization problem, but also serve as a key part of the sensitivity studies on the robustness of the optimal solution. For example, the higher slurry concentration with a relatively fast mass flow rate will increase the system's throughput. However, the resulting short residence time can lead to small crystal sizes, leading to poor filterability and unsatisfactory crystal design. Vice versa, considering that higher cake volume will require extended filtration and drying time, the critical process parameters in the carousel should be decided with a thorough analysis to accommodate the introduced slurry to achieve target CQAs while ensuring not over-processing the cake. The detailed analysis, including all the decision variables in $\boldsymbol{d}$ is consecutively discussed in dynamic simulations on the integrated crystallization-CFC (Section 4.1.3).

From the grid-based simulation result, feasible regions of $\boldsymbol{d}$ are identified and the bounds and initial guess are used to solve the simulation-based optimization problem of Eq. (47)-(52) with a derivative-free Nelder-Mead (NM) algorithm from the SciPy library (Virtanen et al., 2020). After that, we analyze the improved process outputs of the optimized steady-state solutions found. (Section 4.2). The same problem was solved by customizing an accelerated evolutionary optimization algorithm (Storn & Price et al., 1997) to avoid the NM method to getting stuck in a suboptimal solution in the vicinity of the seed value. Given

its stochastic nature, genetic algorithms (GA) serve to evaluate the quality of local solution found by NM by comparing the solutions.

3.3 Sensitivity and robustness study of the optimization

The robustness of the calculated optimal operating conditions needs to be examined for a practical application in future experimental validation, which contains various sources of uncertainty in the purification kinetics. The effect of parametric and operational uncertainty on the optimal design found with NM was tested by means of sensitivity analysis (SA) (Jansen, 1999; Saltelli et al., 2010). The crystallization model includes various input model parameters, such as solubility and kinetic coefficients. These parameters have been calculated from several experiments from the previous literature, where the mean value and confidence interval for the parameters are reported (Szilagyi et al., 2020). The design of the carousel process should also account for process disturbances and uncertainties, such as filter mesh fouling, cleaning in place (CIP), and dynamic variations of slurry from the preceding crystallization step (Destro et al., 2021). The uncertain parameters of the flowsheet model of the integrated purification step for paracetamol are summarized in Table 3. While the uncertainties coming from connection with crystallization has been taken care of by the ‘Connection module’ from PharmaPy, process disturbances still need to be addressed. Thus, SA is performed to quantify the individual contribution of model parameters and rank under each model output to prioritize the significant parameter and reduce the uncertainty propagation within either in-silico Monte Carlo simulation or in-situ experimental design (Helton & Davis, 2003).

In summary, the proposed workflow on digital design of PharmaPy flowsheet simulation is described in Figure 3. First, grid-based simulations are used to compute the design spaces of the crystallization step as well as the integrated crystallization-filtration-drying process, determined by the steady state CQAs, followed by the investigations of the dynamics of the integrated process. Next the digital design of the integrated process is performed using model-based optimization followed by the robustness analysis of the optimized design.

4. Results and Discussion

4.1 Design space investigations using grid-based simulations

All the simulations were performed using PharmaPy developed in Python 3.7 on a laptop with an Intel® core™ i9–9880H CPU and 32.0 GB RAM.

4.1.1 Steady-state design space investigation of the MSMPR cascade—

The impact of CPPs of the crystallization step on maximizing the throughput was examined by evaluating the properties of the slurry from CR02, by performing steady state design space investigations. Slurry concentration (C_{slurry}) and throughput, where the latter is calculated by incorporating transfer mass flow rate ($\dot{F}^{out}_{\mathrm{CR02}}$) (Eq. (45)), are investigated.

Figure 4 presents the coupled effect of temperature of CR01 and residence time of CR01 and CR02 on slurry concentration in the two-stage crystallizer. It is observed that slurry concentration is positively proportionate to the CPPs in crystallization step. This

phenomenon is consistent as the first MSMPR functions primarily as a nucleation vessel. The higher residual supersaturation in the CR01 is created in higher β_{CR01} regime. This results in higher nuclei generation, which will ultimately proceed through to the second stage where growth of crystals is controlled under the remaining supersaturation and residence time. Also, the higher residence time in respective stages of the crystallizer, the more extended time is available for supersaturation to be depleted via crystallization, hence a more concentrated slurry is acquired from the outlet of CR02.

However, higher slurry concentration does not always align with increasing the throughput in the integrated crystallization-filtration-drying system. Here, we define the main process goal as maximizing the mass of crystals transferred in a slurry stream during a single residence time of the crystallization and fast handling of the generated slurry by the carousel, represented as a single cycle (Eq.(47)). Thus, the throughput is calculated by also considering $\dot{F}^{out}_{\mathrm{CR02}}$ and τ_{CR02} with c_{slurry} from the flowsheet simulation for each grid point and plotted in Figure 5. Here, constant values for the CFC CPPs are used to calculate the throughput (Table 4). It can be noticed that increasing τ_{CR01} results in a smaller throughput value, while β_{CR01} and τ_{CR02} have a same trend as shown for c_{slurry}. Hence, for the considered crystallization kinetics, increasing the residence time in the first crystallizer (τ_{CR01}), thus theoretically allowing more solid mass to form by nucleation and/or growth, does not compensate for the reduced $\dot{F}^{out}_{\mathrm{CR02}}$ in improving the overall throughput. This is most likely due to the relatively fast nucleation kinetics of the system, which causes fast depletion of supersaturation in the first crystallizer to levels at which nucleation and growth rate contribute little to increase of mass even at longer residence times. However, it is plausible that other APIs with lower nucleation and higher growth kinetics would increase the throughput by generating more nuclei crystals with the extended τ_{CR01} under the exact condition of the CR02. However, in all cases, the sensitivity of τ_{CR01} to the crystal growth in CR01 should be examined to prevent not only decreasing the throughput but also meeting the target size of the crystal product.

The simulation results using the crystallization subsystem reveal the trends in the properties of the intermediate slurry based on the CPPs of the crystallization step and indicate how these can be chosen to maximize the main objective, the throughput. It can be inferred that the optimal operating conditions β_{CR01} and τ_{CR02} can be set at their corresponding upper bounds, whereas τ_{CR01} lies within the boundaries where the optimal supersaturation can achieve the target goal. The grid-based analysis narrows down the candidate design space for optimal crystallization process design, focusing on the main objective value. The slurry properties predicted from the crystallization step play a crucial role in determining cake properties. This further narrows down the design space by evaluating the filtration-drying process within the defined parameters from the crystallization step. The residence time of CR01 and CR02 is an important factor that affects cake properties such as introduced cake volume, cake porosity, and maximum cycle time during the filtration-drying process. It is necessary to evaluate if any sub-space within the operating regions is preferred for different process goals and gain a deeper understanding of the underlying mechanisms. To truly achieve the goal of maximizing overall throughput and satisfying other critical quality attributes of the products (Eq. 47–51), a crystallization design must be considered

within the context of integrated manufacturing, utilizing the entire flowsheet model of the crystallization process coupled with the filtration and drying processes.

4.1.2 Steady-state design space analysis of the integrated purification step—

The CSD is a critical CQA of the crystallization step and determines the filterability of the wet cake for the filtration and drying processes. The CSDs were identified via flowsheet simulation of the coupled crystallization-CFC process, and Figures 6 depict the dependence of the mean crystal size and cake porosity on three operating variables, β_{CR01}, τ_{CR01}, and τ_{CR02} from the crystallization, respectively. Figure 6.a demonstrates that mean crystal size increases as τ_{CR02} increases, allowing crystals in CR02 more time to grow. Likewise, β_{CR01} was also observed to increase $L_{crystal}$; however, the effect of longer τ_{CR01} to resulting in a bigger mean crystal size only takes into effect at the region of β_{CR01} higher than 0.4. Considering the goal of the integrated purification process is to attain a target crystal size, restrain the final moisture content to the target value, and throughput maximization τ_{CR01} and β_{CR01} needs to be selected simultaneously while ensuring the crystal size and slurry filterability are acceptable. Figure 6.b illustrates how the presence of crystal fines in the slurry affects cake porosity. If τ_{CR01} and τ_{CR02} are too short fines wash out without enough growth taking place. For temperature values in CR01 corresponding to $\beta_{CR01} < 0.4$ the system prefers to put more allocation in τ_{CR02} by sparing τ_{CR01} to generate bigger porosity of the cake. This aligns with the trend of mean crystal size shown in Figure 6.a, where mean crystal size was barely dependent on τ_{CR01}. This implies CR01 does not have enough supersaturation for $\beta_{CR01} < 0.4$, and CR02 turns into a major stage where all crystal kinetics are simultaneously controlled. Meanwhile, the nucleation starts to effectively be controlled in CR01 at $\beta_{CR01} > 0.4$, where global minimum porosity regions are started to get identified (Figure 6.b). The minimum porosity exists at the shorter overall residence time region (bottom-left corner) where the nuclei generated in CR01 leave the crystallizer having too small size and cannot grow larger under the overall short residence time. The porosity becomes larger in operating region of long residence time as either τ_{CR01} and τ_{CR02} increases. It is worth to notice that the τ_{CR02} is more sensitive decision variable to the porosity than τ_{CR01}. This gives an insight of different crystallization kinetic interplay between secondary nucleation and growth in CR02. For $\beta_{CR01} < 0.4$, secondary nucleation dominates the growth in CR02, where it leads to smaller mean crystal size and smaller porosity resulting from the high intermediate crystal fines, whereas $\beta_{CR01} > 0.4$ promotes more growth phenomenon over secondary nucleation.

Figure 7 illustrates the multidimensional design space under four operating variables, β_{CR01}, τ_{CR01}, τ_{CR02}, and T_{drying}, where it shows the final moisture content of the final product after the carousel process completes under a fixed t_{filt} and t_{dry}. The darkest region shows where the operating condition met the lowest saturation value of dry product under 7 %, the grey region is when the saturation value is in between of 7% and 15%, and the rest of the region is when the saturation is above 15%. Higher T_{drying} expands the darkest region by effectively reducing the final saturation value of the cake under constant operating variables. For β_{CR01} values below 0.4, longer τ_{CR01} values result in larger black spaces due to lower flowrate of the slurry introduced to the CFC from the crystallization system. The porosity value and crystal size also become inferior for the filterability because of the fines generated, but smaller

slurry volume introduced compensates for the cake with poor filterability with less cycle time required for less material. As β_{CR01} increases above 0.4, the overall saturation increases throughout the overall residence time with smaller darker region available due to the higher material throughput (Figure 7). Notably, $\beta_{CR01} = 0.4$ corresponds to the temperature triggering nucleation in CR01 from Figure 6. The trend of higher saturation achieved for β_{CR01} values above 0.4 persists despite the better filterability of the cake represented by a higher porosity value. Despite the trend, the operable space emerges again where the porosity is tuned above 0.32 when β_{CR01} is above 0.8. This shows a trade-off between the high throughput and lower final saturation of the dry products in the integrated crystallization-filtration process; however, β_{CR01} can be designed and controlled to improve filterability under a target throughput and product quality goal.

Likewise, it is visible that the longer τ_{CR02} is, the lower the final residual saturation attained under fixed β_{CR01} and τ_{CR01}. This clearly shows the contribution of better filterability represented by higher mean size and porosity even though the slurry concentration is higher for longer τ_{CR02} (Figure 4). Thus, the final saturation design space indicates the region near the lower bound and upper bound of β_{CR01} and higher τ_{CR02} as a preferred operating region of the system to achieve the target saturation value of 5%. The design space analysis demonstrates the impact of operating variables on final moisture content and filterability. The study highlights the trade-off between throughput and product quality, with β_{CR01} playing a crucial role in balancing these factors. Understanding these relationships enables the design and control of the crystallization-filtration process to optimize filterability even for a thicker cake during steady-state operation.

4.1.3 Dynamic analysis of the integrated continuous crystallization-filtration-drying system—For better startup design and more robust operation it is important to understand the dynamic behavior of the integrated system. During the initial transient period, when the average crystal size is below $10\,\mu m$, filterability is significantly lower due to high specific cake resistance value. These crystals require a longer filtration time, but a low concentration of the feed slurry to the carousel will result in a thinner cake to process for a given cycle time. Thus, the counteracting effect of low filterability and thinner cake can be considered together so that the carousel setting is adjusted during the transient period until the preceding crystallization process reaches steady state. This can lead to an optimized start-up procedure that can further increase throughput and minimize off-spec product. Additionally, the operation of the crystallization process can be also optimized to tailor the filterability of the cake in during the transient period.

To analyze the transient behavior of the system, the integrated continuous purification process is evaluated by a dynamic simulation, using a fixed $\beta_{CR01} = 0.6$ ($T_{CR02} = 10$ °C), ΔP =30 kPa, $t_{filt} = t_{drying} = 5$min, $W = 5$, and $T_{drying} = 50\,°C$. A step change is applied to the process, whereby $\tau_{CR01} = \tau_{CR02} = 20\,\mathrm{min}$ is stepped at the 20^{th} residence time of the process to $\tau_{CR01} = \tau_{CR02} = 40$ min and simulated for another 20 residence times as shown in Figure 8.a. Thus, a total of 20-hour continuous purification platform operation was simulated, with a total computation time of 38.3 minute. A total of 228 slurry batches are processed during

the simulation in the carousel, which processes the slurry generated from the preceding crystallization following the simulation executive structure shown in Figure 2.

During the initial startup of the crystallizer (corresponding 1st residence time of simulation), no significant number of crystals were detected at the outlet of the CR02, ($L_{crystal} < 0.99\,\mu m$) (Figure 8), and consequently the carousel was not processing any detectable quantity of dried product. After this induction time, crystal products generated from the crystallization are further processed in the carousel. The residual mean moisture content ($S_{cake,\,dry}$), after the deliquoring and drying steps taking place every carousel cycle, is shown in Figure 8.b. As the wet cake is further processed within a carousel cycle, a lower saturation value is achieved. Before the step change on τ_{CR01} and τ_{CR02} occur (Figure 8.a), $S_{cake,\,dry}$ is kept under 5% v/v and then it progressively increases until reaching 6.4 % v/v, where a new steady state is attained. Both final saturation and filtration time increase after the introduced step change in the crystallization residence times, since lower liquid flow across the cake leads to less efficient deliquoring process.

Cake resistivity (α_{cake}) (Figure 8.d) shows a sudden decrease from $2.6 \times 10^{11}\,m/kg$ to $2.7 \times 10^{11}\,m/kg$ due to the generation of more fine particles resulting from the introduced step change, decreasing slowly but constantly to $2.3 \times 10^{11}\,m/kg$ as the crystals grow and settle to a new steady state. The steady state value of the slurry concentration (C_{slurry}) is increased to 39 kg/m^3 after the step change from 0.07 kg/m^3, as seen in Figure 8.f. Also, the time required for filtration process (t_F) to finish recorded and plotted in Figure 8.c.

While the increment of C_{slurry} is about 550-fold, the steady state t_F is expected to be increased only about 4 times of the value (23 sec) before the step changes as a result of lower cake resistance. Also, the reduced flow rate at which the slurry is introduced into the carousel port contributed to shortening filtration time.

Figure 8.b demonstrates, for the given carousel setting, the improved efficiency of deliquoring after the step increase in the crystallizer residence times. Besides a smaller introduced slurry volume from a reduced flowrate, the lower steady-state specific cake resistivity, also caused by larger mean crystal size ($L_{crystal}$), also contributed to higher liquid removal between DL01 and DL02. This illustrates how the property of the filter cake can be adjusted to expedite the solid-liquid separation process in the case of a more concentrated slurry by manipulating the upstream control variables of the crystallization step. Herein, the importance of having an appropriate target steady-state mean crystal size, is emphasized since it contributes to critical cake properties, α and ϵ, which are critical parameters to enhance the filterability of the cake.

It is worth to note, at the first carousel batch after the step change (6.6 hour), the t_F showed a significant improvement from 42.1 s to 11.7 s due to a reduced $\dot{F}^{out}_{\mathrm{CR02}}$, while C_{slurry} and α_{cake} both increased, whereas $L_{crystal}$ and ϵ decreased as a result of the voids of the filter cake being filled with small fines produced (Figure 8). This means that the reduced slurry cake amount introduced into the carousel batch does not require the entire duration of pre-defined cycle time despite the poor cake properties during this transient period. Then, to improve

the throughput value, the t_{filt} and t_{dry} can be adjusted to not exceed the necessary t_F until the process reaches a new steady state. Understanding and prediction the dynamics of the integrate system implies that the carousel operating variables can be actively adjusted to improve the throughput during the transient period. However, in order to design the steady state performance of the coupled crystallizer and CFC, the parameters directly coming from crystallizer operating variables ($\dot{F}^{out}_{\mathrm{CR02}}$, $L_{crystal}$, and C_{slurry}) and cake parameters (ε and α_{cake}) calculated from the slurry CSD should be all accounted simultaneously to achieve target moisture content and maximization of throughput.

4.2 Digital-design of the integrated crystallization-filtration-drying system

Based on understanding the overall feasible design space using the integrated flowsheet simulations, a digital design framework is implemented using a sequential simulation-optimization approach. The gradient-free direct search method is implemented to minimize the objective function from outputs obtained by callbacks on the PharmaPy flowsheet simulation every iteration (Eq.(59)). The decision variables have been scaled in the interval of 0 to 1, considering the difference in orders of magnitude among different variables for the optimizer algorithm (Eq. (58)). The algorithm updates the scaled decision variables ($\bar{d}_p$) and translates back to original $d_p = [\beta_{CR01}, \tau_{CR01}, \tau_{CR02}, t_{filt}, t_{drying}, \Delta\mathrm{P}, W, T_{drying}]$ for evaluating the augmented objective after modifying its simplex at each iteration (Eq. (59)). The inequality constraints have been included in the objective function via a penalty term, where $\boldsymbol{P}$ is a suitable weighing matrix, $f(d_p)$ is the original objective function which is overall throughput, $g(d_p)$ is the calculated CQAs, and g_{target} is the reference target value for the inequality constraints.

$$\bar{d}_p = \frac{d_p - d_{lb,\,p}}{d_{ub,\,p} - d_{lb,\,p}} \tag{58}$$

$$\min_{d_p \in d} \left\{ f(d_p) + max\left(0, (g(d_p) - g_{target})^T P (g(d_p) - g_{target})\right) \right\} \tag{59}$$

The optimization solution and simulated outputs are presented in Table 5 and Table 6, respectively. Both optimization methods yield similar solutions, indicating the likelihood of finding the global optimum. This verifies the robustness of PharmaPy's single objective with penalty terms representing multiple constraints. In the crystallization system, the optimal τ_{CR02} is much longer than τ_{CR01}, suggesting the first crystallizer functions as a nucleation vessel while the second facilitates crystal growth. At the same time, the yield of the crystallization is improved to suffice the yield criteria. The value of β_{CR01} is set to its upper bound to achieve 90% target yield without compromising throughput by allocating excessively long residence time in CR01. Crystal kinetics are depicted in Figure 9, showing higher nucleation and growth rates in CR01 to CR02 due to greater supersaturation.

However, the nucleation becomes the primary kinetic in CR01 under shorter residence time, allowing residual supersaturation in CR02 to promote crystal growth and minimize the generation of nuclei to achieve the target mean size.

Among the control variables of the carousel unit, maximizing ΔP and T_{drying} enhances convective flow and thermal drying. The W is optimized to reduce uptake of the original mother liquor during washing. For t_{filt} and t_{drying}, their values of 50s and 150s, respectively, are set to introduce sufficient slurry volume and cycle time to achieve the desired throughput and target moisture content.

The NM method's optimal design significantly improves throughput from 0.19 kg/h to 0.676 kg/h, representing a 3.5-fold increase in productivity. Crystal size and slurry volume adhere to specifications, while yield and saturation constraints are active within numerical precision ($g(d_p)$ = 89.99 and 0.0501, respectively). The GA solution yields slightly lower throughput than NM but satisfies inequality constraints with smaller penalties, resulting in an equivalent augmented minimum due to the use of a penalty method. Yield and saturation values remain well within the target boundaries, and crystal size and slurry volume meet the predefined constraints without exceeding the goals.

Notably, the washing ratio differs between the two optimization algorithms. If the filter cake is both washed and deliquored, the passage of gas through the cake reduces the drainage flowrate of the mother liquor, as gas predominantly flows through open pores rather than displacing the mother liquor (Price et al., 2020). Consequently, the remaining fraction of the mother liquor plateaus after a certain washing ratio is applied to the cake. For the given process with a filter cake height less than 5 cm, the critical washing ratio is implied to be a maximum of 2.5. Since both algorithms found a washing ratio greater than 2.5, it becomes a less decisive operating variable as long as an adequate amount of washing solvent is employed to expedite the subsequent drying process by modifying the liquid composition to a more volatile solvent during the washing step.

4.3 Robustness analysis of the digital design

The nominal optimization result was examined by accounting for the uncertainty of the model parameters to verify robustness of the optimal decision variables (Szilagyi et al., 2020). Table 3 summarizes the significant crystallization kinetic parameters, k_p, p, k_s, s, k_g, g, and their 95 % confidence intervals. There are also additional four model parameters from the carousel, R_m, $R_{m,\,dry}$, h_M, h_T, which were estimated from experimental data (Destro et al., 2021; Seader and Henley, 1998). Mesh resistance, R_m and $R_{m,\,dry}$ are considered randomly distributed, with deviation equal to 10 % of the nominal values and mass and heat transfer coefficient, h_M and h_T, are treated with deviations equal to 20 % of their corresponding nominal values. The evaluated parameters were set as uniform distribution of a 10-dimensional input space, aiming to generate non-biased sensitivity results when inputs are expected to be highly uncertain.

Variance-based methods are used for SA with 1000 random samples ($N_{sampling}$) from the defined input parameter uncertainty. The PharmaPy flowsheet model was simulated 1000

times for each realization of the sampled parameters. The primary objective function (throughput) and inequality constraints (yield, mean size, saturation, and slurry volume) are recorded for each simulation, and the resulting dynamic responses are shown in Figure 9.a. Since the physical slurry volume constraint (Eq. (51)) is satisfied with the smaller slurry volume than the 50% occupancy of the maximum capacity of the port, the SA result is abbreviated here, assuming the constraints can be confidently met under the parametric uncertainty. Figure 9.a presents mean value of the dynamic process outcome and variations in 25 percentile intervals. It is shown clearly that the uncertainties in kinetic parameters and specified variations in model parameters are very small for throughput, yield, and mean size under the fixed value of the optimized operation parameters (Section 4.2) not only during steady state but also during the initial dynamic start-up period. The steady-state values of the respective outputs are averaged. Among the steady state outputs, the final saturation was the most uncertain output with mean value of 0.050 and minimum and maximum achieved final saturation of 0.038 and 0.067, respectively, compared to the other outputs with covariance values ranging in the order from 1×10^{-4} to 1×10^{-3}. This implies that achieving the target residual moisture content can be critical and possibly a condition, which will need to be monitored and tightly tuned according to the changes of model parameters so that the process operates successfully in practice.

However, given overall low uncertainties in the process performances (outcomes) from specified variations in the operation design space the resulting process design using the flowsheet model is shown to be robust, generally indicating narrower uncertainty distributions of the outputs than those of the model inputs.

Variance-based sensitivity analysis was performed to indicate which operation input parameter would be the primary driver of uncertainty under a particular steady-state operation (Jansen, 1999; Saltelli et al., 2010). Total sensitivity indices (S_{Ti}) are calculated to measure first and higher-order effects of a parameter, utilizing the flowsheet as a platform to perform Monte Carlo based estimation. A total of 11,000 input vectors were created for the model evaluations, 1000× (10+1), including 1000 vector used on the dynamic response study plotted in Figure 9.a. As a result, total sensitivity indices are calculated and ranked from the most significant contribution to the smallest on specific process output variability (Table 7).

The result shows that the objective values calculated from the crystallization step, i.e., throughput, yield, and mean size, are most sensitive to the secondary nucleation rate constant followed by the growth rate constant (Figure 9.b). This fact can be attributed to the expected mechanism in CR01 where secondary nucleation occurs, followed by the growth. The design of the crystallizer produces an aggressive initial cooling to trigger primary nucleation in CR01 (Table 5).

As shown in Figure 10, by setting a cooling temperature of CR01 as low as possible, the largest supersaturation on CR01 is imposed, and higher nucleation rate is observed in CR01 to that of CR02. Meanwhile, the residence time in CR01 functions as a critical decision variable to decide the residual supersaturation in CR02. Here, it is maintained at 44 min to attain two different goals: (i) sparing enough supersaturation in CR02 for the crystal growth

in the second crystallizer to attain the target crystal size goal by restricting nucleation at CR01; and (ii) allow enough time in CR01 for nucleation to maximize the throughput. The residual supersaturation consumed by generating fines in CR01 will increase the yield/throughput. However, it will hamper the dominance of growth mechanism in CR02, resulting in smaller crystal size to the target. Also, the growth rate coefficient directly dictates the crystal growth rate where the supersaturation is consumed, and this links both to the mean size of the crystal and the yield criteria. The final saturation of the cake is found to be most sensitive to the mass transfer coefficient and heat transfer coefficient, which again emphasizes the significance of the efficient drying of a cake to reduce the moisture content below the saturation value for the cake. The ranking is attained under the optimized filtration and drying cycle time, which decides the slurry volume introduced for the carousel and cycle time to process the wet cake, putting more weights on the drying operation to calculate the final saturation value. In other words, the uncertainties of the filter mesh resistance have been assimilated within the dryer simulation using the optimized filtration and drying cycle time as an input. Under the scenario where the filtration-drying cycle time, which is a critical decision variable for carousel operation, is also an uncertain operating parameter, filter mesh resistance is expected to play a more critical role than the analysis indicated for this study. The results demonstrate how the digital twin of a novel integrated crystallization-filtration-washing-drying process can be used for better understanding the design and operating space of the unit and for the efficient digital design of the purification process.

5. Conclusions

In this study, a comprehensive mechanistic model was introduced that can be used as an analytical tool for advancing pharmaceutical purification process development that consists of integrated crystallization, filtration, washing and drying steps. The dynamic models are implemented in the open-source pharmaceutical model library and simulation environment PharmaPy, and are based on mechanistic models of the purification process considering multi-phase, multi-component systems, allowing flexibility to access the full information of the materials and unit operations participating in the system. The paper introduces an integrated flowsheet simulator of an intensified continuous purification platform, which consisted of a 2-stage crystallization process and a carousel type filtration-washing-drying unit, tailored to address the complexities of continuous pharmaceutical purification. Using the flowsheet process simulator, the steady-state design space (SSDS) of the overall process was determined using a grid-based sampling. The fact that all models in the flowsheet are implemented as dynamic models, enabled the prediction of dynamic behavior of the integrated system. The results demonstrated the importance of integrated process design by demonstrating the coupled relationship between the slurry properties (e.g., slurry concentration, throughput, crystal size, flow rate) with filterability and drying efficiency. Based on the understanding of the SSDS, the dynamic trajectories between two operating points are also investigated, showing that the throughput maximization is feasible under the specified target value for the CQAs throughout the dynamic operations. Finally, two different optimization approaches were evaluated in the optimal digital design of the process, with the objective to achieve maximum steady state throughput while process

constraints (final crystal and dry product CQAs, targeted yield, and capacity of the physical unit) are successfully satisfied.

The paper underscores the pivotal importance of integrated flowsheet simulations as invaluable platforms for the holistic evaluation of process designs in continuous manufacturing systems, demonstrating the role of flowsheet simulators in advancing pharmaceutical process development. Although the presented process design was developed for a steady state process design, the evaluation of utilization of the flowsheet as a dynamic digital twin with the capability of real-time data integration will be performed in the future. This will allow the PharmaPy flowsheet simulation to serve as a modeling framework to develop a dynamic digital twin of the real plant, whereby the model is updated in real-time based on measurements, addressing various process disturbances present in practice.

Supplementary Material

Refer to Web version on PubMed Central for supplementary material.

Acknowledgement.

This project was supported by the United States Food and Drug Administration through grant U01FD006738. The views expressed by the authors do not necessarily reflect official policies of the Department of Health and Human Services; nor does any mention of trade names, commercial practices, or organization imply endorsement by the United States Government.

References

Acevedo D, Peña R, Yang Y, Barton A, Firth P, & Nagy ZK (2016b). Evaluation of mixed suspension mixed product removal crystallization processes coupled with a continuous filtration system. Chemical Engineering and Processing: Process Intensification, 108, 212–219. 10.1016/j.cep.2016.08.006

FDA. (2004). Guidance for Industry, PAT-A Framework for Innovative Pharmaceutical Development, Manufacturing and Quality Assurance. September. http://www.fda.gov/downloads/Drugs/GuidanceComplianceRegulatoryInformation/Guidances/ucm070305.pdf

Boukouvala F, Chaudhury A, Sen M, Zhou R, Mioduszewski L, Ierapetritou MG, & Ramachandran R (2013). Computer-aided flowsheet simulation of a pharmaceutical tablet manufacturing process incorporating wet granulation. Journal of Pharmaceutical Innovation, 8(1), 11–27. 10.1007/s12247-012-9143-9

Boukouvala F, Niotis V, Ramachandran R, Muzzio FJ, & Ierapetritou MG (2012). An integrated approach for dynamic flowsheet modeling and sensitivity analysis of a continuous tablet manufacturing process. Computers and Chemical Engineering, 42, 30–47. 10.1016/j.compchemeng.2012.02.015

Bourcier D, Féraud JP, Colson D, Mandrick K, Ode D, Brackx E, & Puel F (2016). Influence of particle size and shape properties on cake resistance and compressibility during pressure filtration. Chemical Engineering Science, 144, 176–187. 10.1016/j.ces.2016.01.023

Capellades G, Neurohr C, Azad M, Brancazio D, Rapp K, Hammersmith G, & Myerson AS (2020). A Compact Device for the Integrated Filtration, Drying, and Mechanical Processing of Active Pharmaceutical Ingredients. Journal of Pharmaceutical Sciences, 109(3), 1365–1372. 10.1016/j.xphs.2019.12.011 [PubMed: 31866299]

Casas-Orozco D, Laky D, Wang V, Abdi M, Feng X, Wood E, Laird C, Reklaitis G. v., & Nagy ZK (2021). PharmaPy: An object-oriented tool for the development of hybrid pharmaceutical flowsheets. Computers and Chemical Engineering, 153, 107408. 10.1016/j.compchemeng.2021.107408 [PubMed: 38235368]

Chhabra RP, & Shankar V (2017). Coulson and Richardson's Chemical Engineering. Elsevier.

Citti C, Pacchetti B, Vandelli MA, Forni F, & Cannazza G (2018). Analysis of cannabinoids in commercial hemp seed oil and decarboxylation kinetics studies of cannabidiolic acid (CBDA). Journal of Pharmaceutical and Biomedical Analysis, 149, 532–540. 10.1016/j.jpba.2017.11.044 [PubMed: 29182999]

Destro F, Hur I, Wang V, Abdi M, Feng X, Wood E, Coleman S, Firth P, Barton A, Barolo M, & Nagy ZK (2021). Mathematical modeling and digital design of an intensified filtration-washing-drying unit for pharmaceutical continuous manufacturing. Chemical Engineering Science, 244, 116803. 10.1016/j.ces.2021.116803 [PubMed: 38229929]

Destro F, Barolo M, & Nagy ZK (2022a). Quality-by-control of intensified continuous filtration-drying of active pharmaceutical ingredients. AIChE Journal, June, 1–21. 10.1002/aic.17926

Destro F, Nagy ZK, & Barolo M (2022b). A benchmark simulator for quality-by-design and quality-by-control studies in continuous pharmaceutical manufacturing – Intensified filtration-drying of crystallization slurries. Computers and Chemical Engineering, 163. 10.1016/j.compchemeng.2022.107809

Dodda AG, Saranteas K, & Henson MA (2015). Using online mass spectrometry to predict the end point during drying of pharmaceutical products. Organic Process Research and Development, 19(1), 122–131. 10.1021/op400272t

Domokos A, Nagy B, Gyürkés M, Farkas A, Tacsi K, Pataki H, Liu YC, Balogh A, Firth P, Szilágyi B, Marosi G, Nagy ZK, & Nagy ZK (2020). End-to-end continuous manufacturing of conventional compressed tablets: From flow synthesis to tableting through integrated crystallization and filtration. International Journal of Pharmaceutics, 581(March), 119297. 10.1016/j.ijpharm.2020.119297 [PubMed: 32243964]

Dullien FL (1992) Fluid Transport and Pore Structure. Academic, New York.

Endo Y, & Alonso M (2001). Physical meaning of specific cake resistance and effects of cake properties in compressible cake filtration. Filtration and Separation, 38(7), 42–46. 10.1016/S0015-1882(01)80447-X

Eriksson G, Rasmuson A, & Theliander H (1996). Displacement washing of lime mud: Tailing effects. Separations Technology, 6(3), 201–210. 10.1016/0956-9618(96)00154-3

European Medicines Agency. (2019). ICH guideline Q3C (R6) on impurities: Guideline for Residual Solvents. International Conference on Harmonization of Technical Requirements for Registration of Pharmaceuticals for Human Use, 31(August), 24.

García-Muñoz S, Butterbaugh A, Leavesley I, Manley LF, Slade D, & Bermingham S (2018). A flowsheet model for the development of a continuous process for pharmaceutical tablets: An industrial perspective. AIChE Journal, 64(2), 511–525. 10.1002/aic.15967

Granberg RA and Rasmuson ÅC (1999) Solubility of Paracetamol in Pure Solvents. Journal of Chemical & Engineering Data, 44, 1391–1395. 10.1021/je990124v

Gunawan R, Fusman I, & Braatz RD (2004). High resolution algorithms for multidimensional population balance equations. AIChE Journal, 50(11), 2738–2749. 10.1002/aic.10228

Habicht J, & Wohlgemuth K (2022). Continuous Isolation of Particles with Varying Aspect Ratios up to Thin Needles Achieving Free-Flowing Products.

Helton JC, & Davis FJ (2003). Latin hypercube sampling and the propagation of uncertainty in analyses of complex systems. Reliability Engineering and System Safety, 81(1), 23–69. 10.1016/S0951-8320(03)00058-9

Hindmarsh AC, Brown PN, Grant KE, Lee SL, Serban R, Shumaker DANE, & Woodward CS (2005). SUNDIALS : Suite of Nonlinear and Differential / Algebraic Equation Solvers. 31(3), 363–396.

ICH Quality Implementation Working Group. Point to Consider: ICH-endorsed Guide for ICH Q8/Q9/Q10 Implementation. 2011.

Jansen MJW (1999). Analysis of variance designs for model output. Computer Physics Communications, 117(1), 35–43. 10.1016/S0010-4655(98)00154-4

Jolliffe HG, & Gerogiorgis DI (2017). Technoeconomic Optimization of a Conceptual Flowsheet for Continuous Separation of an Analgaesic Active Pharmaceutical Ingredient (API). Industrial and Engineering Chemistry Research, 56(15), 4357–4376. 10.1021/acs.iecr.6b02146

Jung JY, Blau G, Pekny JF, Reklaitis GV, & Eversdyk D (2004). A simulation based optimization approach to supply chain management under demand uncertainty. Computers and Chemical Engineering, 28(10), 2087–2106. 10.1016/j.compchemeng.2004.06.006

Kaialy W, Alhalaweh A, Velaga SP, & Nokhodchi A (2012). Influence of lactose carrier particle size on the aerosol performance of budesonide from a dry powder inhaler. Powder Technology, 227, 74–85. 10.1016/j.powtec.2012.03.006

Lapidus L, & Amundson NR (1952). Mathematics of adsorption in beds. VI. The effect of longitudinal diffusion in ion exchange and chromatographic columns. Journal of Physical Chemistry, 56(8), 984–988. 10.1021/j150500a014

Leveque RJ (2002) Finite Volume Methods for Hyperbolic Problems. Cambridge University Press, Cambridge. 10.1017/CBO9780511791253

Levi-Hevroni D, Levy A, & Borde I (1995). Mathematical modeling of drying of liquid/solid slurries in steady state one-dimensional flow. Drying Technology, 13(5–7), 1187–1201. 10.1080/07373939508917016

Liu YC, Domokos A, Coleman S, Firth P, & Nagy ZK (2019). Development of Continuous Filtration in a Novel Continuous Filtration Carousel Integrated with Continuous Crystallization. Organic Process Research and Development, 23(12), 2655–2665. 10.1021/acs.oprd.9b00342

Liu YC, Dunn D, Lipari M, Barton A, Firth P, Speed J, Wood D, & Nagy ZK (2019). A comparative study of continuous operation between a dynamic baffle crystallizer and a stirred tank crystallizer. Chemical Engineering Journal, 367(September 2018), 278–294. 10.1016/j.cej.2019.02.129

Maloney AJ, Içten E, Capellades G, Beaver MG, Zhu X, Graham LR, Brown DB, Griffin DJ, Sangodkar R, Allian A, Huggins S, Hart R, Rolandi P, Walker SD, & Braatz RD (2020). A Virtual Plant for Integrated Continuous Manufacturing of a Carfilzomib Drug Substance Intermediate, Part 3: Manganese-Catalyzed Asymmetric Epoxidation, Crystallization, and Filtration. Organic Process Research and Development, 24(10), 1891–1908. 10.1021/acs.oprd.0c00189

Muskat M, & Meres MW (1936). The flow of heterogeneous fluids through porous media. Journal of Applied Physics, 7(921), 346–363. 10.1063/1.1745403

Nagy B, Szilágyi B, Domokos A, Tacsi K, Pataki H, Marosi G, Nagy ZK, & Nagy ZK (2020). Modeling of pharmaceutical filtration and continuous integrated crystallization-filtration processes. Chemical Engineering Journal, November. 10.1016/j.cej.2020.127566

Nagy B, Szilágyi B, Domokos A, Tacsi K, Pataki H, Marosi G, Nagy ZK, & Nagy ZK (2021). Modeling of pharmaceutical filtration and continuous integrated crystallization-filtration processes. Chemical Engineering Journal, 413(October 2020). 10.1016/j.cej.2020.127566

Nagy B, Szilágyi B, Domokos A, Vészi B, Tacsi K, Rapi Z, Pataki H, Marosi G, Nagy ZK, & Nagy ZK (2021). Dynamic flowsheet model development and digital design of continuous pharmaceutical manufacturing with dissolution modeling of the final product. Chemical Engineering Journal, 419(April). 10.1016/j.cej.2021.129947

Öner M, Stocks SM, & Sin G (2020). Comprehensive sensitivity analysis and process risk assessment of large scale pharmaceutical crystallization processes. Computers and Chemical Engineering, 135. 10.1016/j.compchemeng.2020.106746

Ottoboni S, Price CJ, Steven C, Meehan E, Barton A, Firth P, Mitchell A, & Tahir F (2019). Development of a Novel Continuous Filtration Unit for Pharmaceutical Process Development and Manufacturing. Journal of Pharmaceutical Sciences, 108(1), 372–381. 10.1016/j.xphs.2018.07.005 [PubMed: 30009797]

Ottoboni S, Brown CJ, Mehta B, Jimeno G, Mitchell NA, Sefcik J, & Price CJ (2022). Digital Design of Filtration and Washing of Active Pharmaceutical Ingredients via Mechanistic Modeling. Organic Process Research and Development. 10.1021/acs.oprd.2c00165

Ouchlyama N, & Tanaka T (1986). Porosity estimation from particle size distribution. Industrial and Engineering Chemistry Fundamentals, 25(1), 125–129. 10.1021/i100021a019

Plumb K (2005). Continuous processing in the pharmaceutical industry: Changing the mind set. Chemical Engineering Research and Design, 83(6 A), 730–738. 10.1205/cherd.04359

Reynolds T, Boychyn M, Sanderson T, Bulmer M, More J, & Hoare M (2003). Scale-Down of Continuous Filtration for Rapid Bioprocess Design: Recovery and Dewatering of Protein Precipitate Suspensions. 10.1002/bit.10687

Price CJ, Barton A, & Coleman SJ (2020). CHAPTER 13. Continuous Isolation of Active Pharmaceutical Ingredients. In The Handbook of Continuous Crystallization. The Royal Society of Chemistry. 10.1039/9781788013581-00469

Randolph AD, & Larson MA (1971). The steady-state MSMPR Crystallizer. Theory of Particulate Processes, 64–78. 10.1016/b978-0-12-579650-7.50009-9

Saltelli A, Annoni P, Azzini I, Campolongo F, Ratto M, & Tarantola S (2010). Variance based sensitivity analysis of model output. Design and estimator for the total sensitivity index. Computer Physics Communications, 181(2), 259–270. 10.1016/j.cpc.2009.09.018

Schaber SD, Gerogiorgis DI, Ramachandran R, Evans JMB, Barton PI, & Trout BL (2011). Economic analysis of integrated continuous and batch pharmaceutical manufacturing: A case study. Industrial and Engineering Chemistry Research, 50(17), 10083–10092. 10.1021/ie2006752

Seader JD, Henley EJ, & Roper DK (2016). Separation process principles: With applications using process simulators. John Wiley & Sons.

Storn R, Price K Differential Evolution – A Simple and Efficient Heuristic for global Optimization over Continuous Spaces. Journal of Global Optimization 11, 341–359 (1997). 10.1023/A:1008202821328

Sen M, Rogers A, Singh R, Chaudhury A, John J, Ierapetritou MG, & Ramachandran R (2013). Flowsheet optimization of an integrated continuous purification-processing pharmaceutical manufacturing operation. Chemical Engineering Science, 102, 56–66. 10.1016/j.ces.2013.07.035

Sen M, Singh R, & Ramachandran R (2014). A Hybrid MPC-PID control system design for the continuous purification and processing of active pharmaceutical ingredients. Processes, 2(2), 392–418. 10.3390/pr2020392

Simon LL, Kiss AA, Cornevin J, & Gani R (2019). Process engineering advances in pharmaceutical and chemical industries: digital process design, advanced rectification, and continuous filtration. Current Opinion in Chemical Engineering, 25, 114–121. 10.1016/j.coche.2019.02.005

Steenweg C, Kufner AC, Habicht J, & Wohlgemuth K (2021). Towards Continuous Primary Manufacturing Processes—Particle Design through Combined Crystallization and Particle Isolation. Processes, 9(12), 2187. 10.3390/pr9122187

Stephanopoulos G, & Reklaitis GV (2011). Process systems engineering: From Solvay to modern bio- and nanotechnology.. A history of development, successes and prospects for the future. Chemical Engineering Science, 66(19), 4272–4306. 10.1016/j.ces.2011.05.049

Szilagyi B, Eren A, Quon JL, Papageorgiou CD, & Nagy ZK (2020). Application of Model-Free and Model-Based Quality-by-Control (QbC) for the Efficient Design of Pharmaceutical Crystallization Processes. Crystal Growth and Design, 20(6), 3979–3996. 10.1021/acs.cgd.0c00295

Tarleton ES, Wakeman RJ, 2007. 6 - Process design for batch separations, in: Tarleton ES, Wakeman RJ (Eds.), Solid/Liquid Separation. Butterworth-Heinemann, Oxford, pp. 256–328.

Virtanen P, Gommers R, Oliphant TE, Haberland M, Reddy T, Walt SJ Van Der, Brett M, Wilson J, & Millman KJ (2020). computing in Python. 17(March). 10.1038/s41592-019-0686-2

Wakeman RJ (1979). Low-pressure dewatering kinetics of incompressible filter cakes, I. Variable total pressure loss or low-capacity systems. International Journal of Mineral Processing, 5(4), 379–393. 10.1016/0301-7516(79)90046-2

Ward JD, Yu CC, & Doherty MF (2011). Analytical design and operation of systems with crystallization, filtration, and recycling. Industrial & engineering chemistry research, 50(3), 1196–1205.

Wood B, Girard KP, Polster CS, & Croker DM (2019). Progress to Date in the Design and Operation of Continuous Crystallization Processes for Pharmaceutical Applications. Organic Process Research and Development, 23(2), 122–144. 10.1021/acs.oprd.8b00319

Yang X, Acevedo D, Mohammad A, Pavurala N, Wu H, Brayton AL, Shaw RA, Goldman MJ, He F, Li S, Fisher RJ, O'Connor TF, & Cruz CN (2017). Risk Considerations on Developing a Continuous Crystallization System for Carbamazepine. Organic Process Research and Development, 21(7), 1021–1033. 10.1021/acs.oprd.7b00130

Yu AB, Zou RP, & Standish N (1996). Modifying the linear packing model for predicting the porosity of nonspherical particle mixtures. Industrial and Engineering Chemistry Research, 35(10), 3730–3741. 10.1021/ie950616a

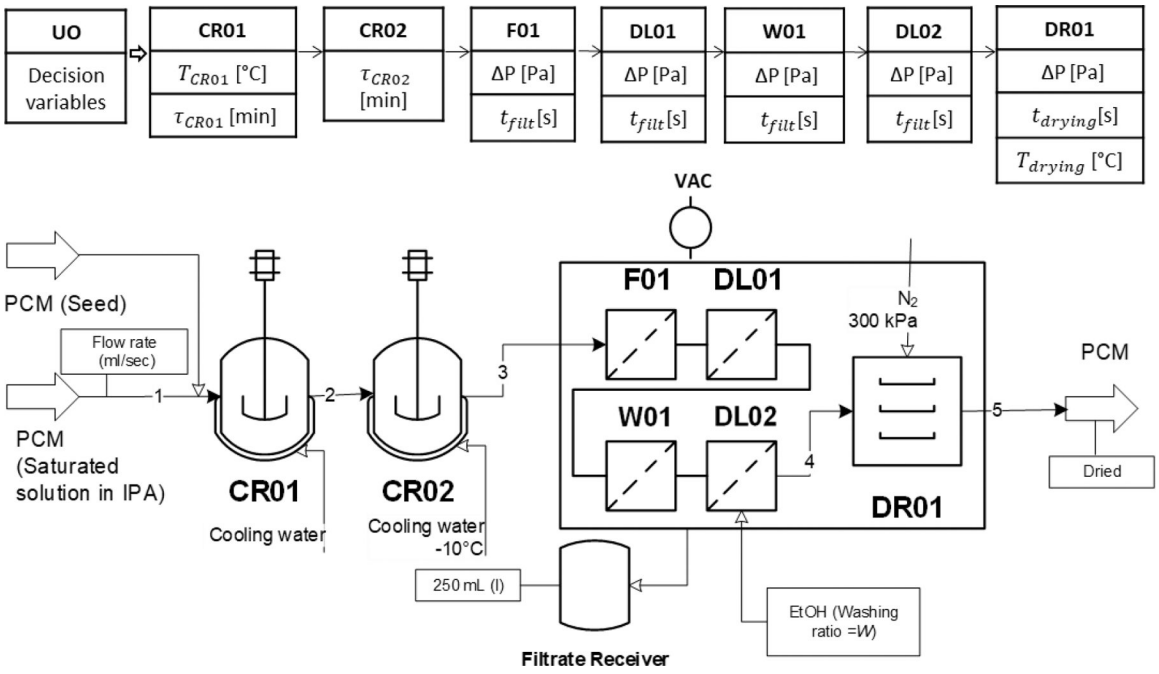

Figure 1:

Process flow diagram for integrated crystallization-filtration-drying platform for the API and corresponding decision variables on each unit operations (UOs). Summary of decision variables of the flowsheet is summarized in Table 2.

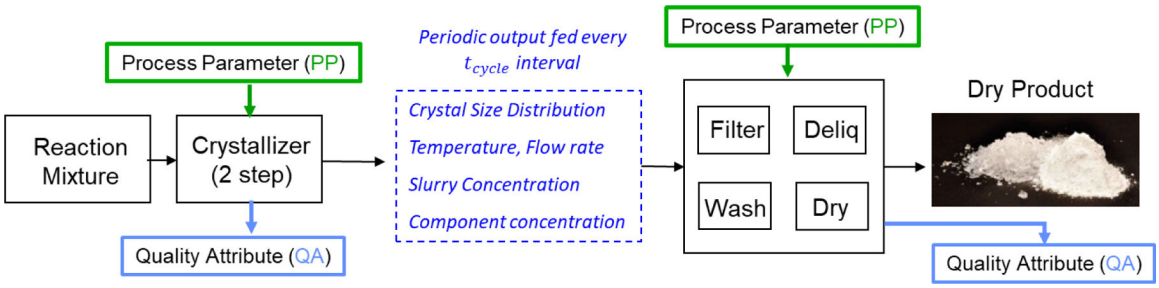

Figure 2.

Flow diagram of the simulation executives of the digital twin of sequential batch simulation for filtration-drying with continuous crystallization process

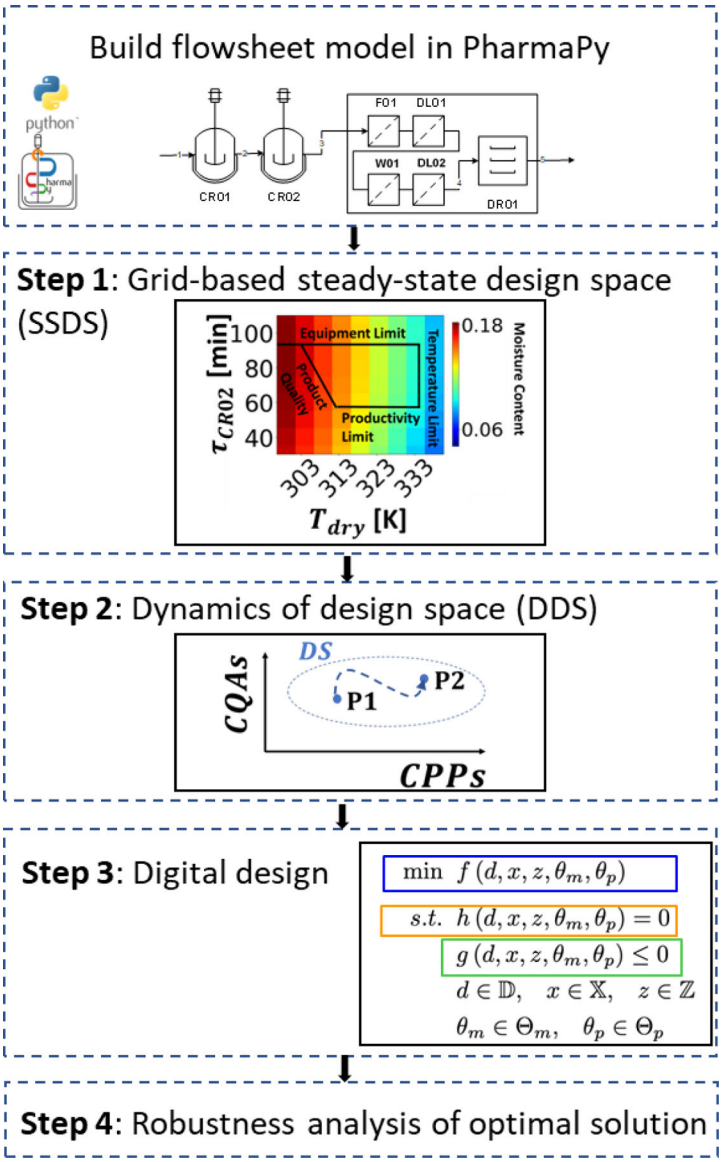

Figure 3.

The process development of model-driven pharmaceutical manufacturing involves four steps: 1) building the flowsheet model, 2) implementing steady-state design space (SSDS) using grid-based sampling, 3) analyzing the trajectory of dynamics between operating points, and 4) optimizing the digital design. The SSDS and DDS provide an initial operating space for the optimization problem, and the flowsheet model is solved again to map process output robustness under parametric uncertainties.

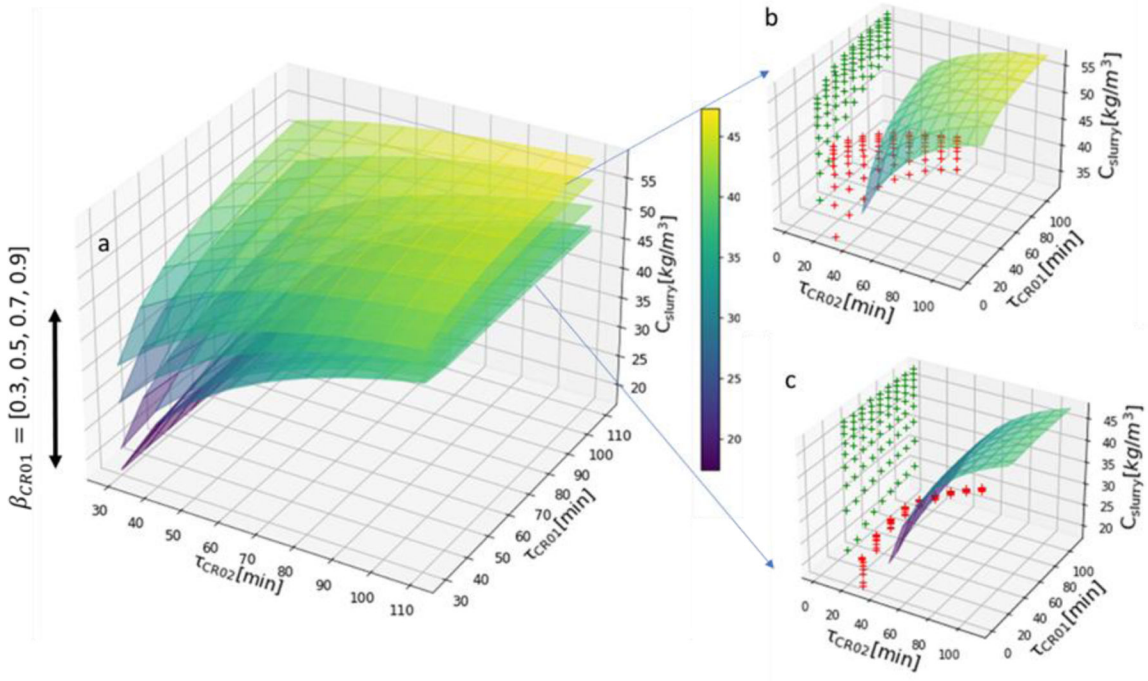

Figure 4.

(a) Effect of residence time of CR01, CR02, and temperature drop ratio of CR01 on slurry concentration. Each plane represents results from the constant temperature drop ratio. (b) Projection of contours on different faces when $\beta_{CR01} = 0.9$. (c) Projection of contours on different faces when $\beta_{CR01} = 0.3$

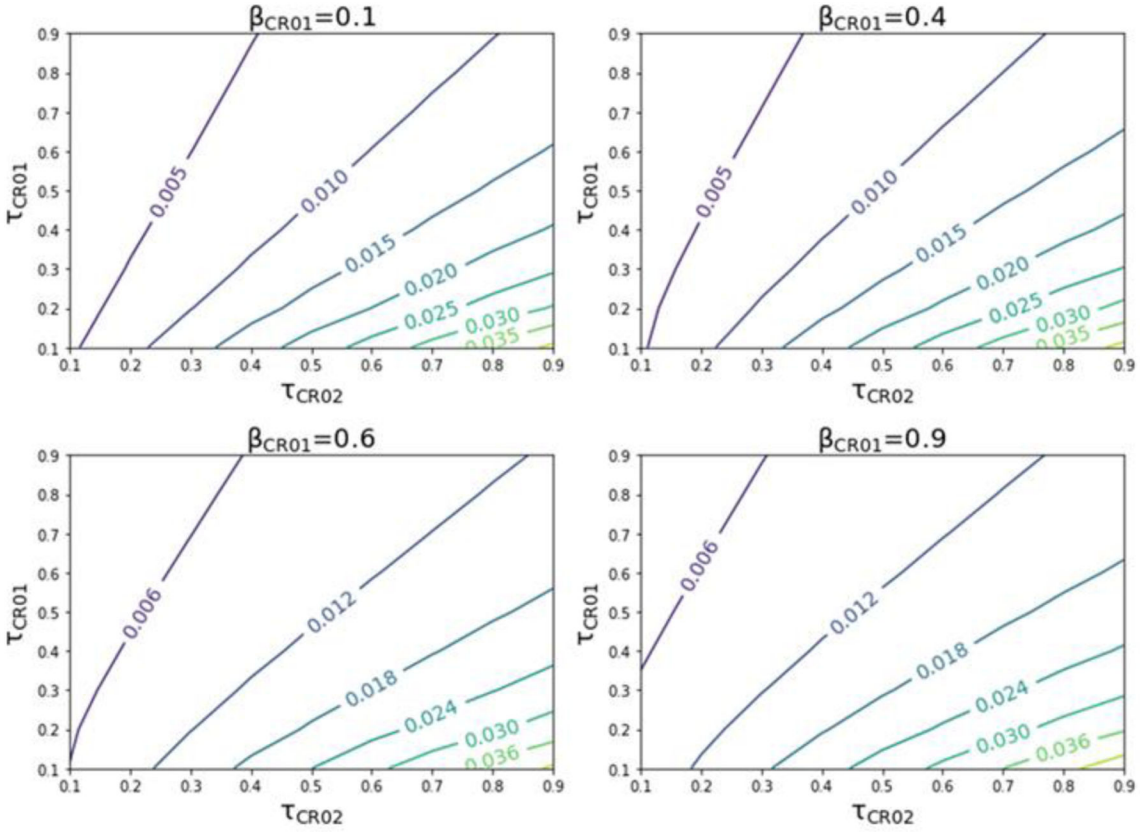

Figure 5.

Effect of residence time of CR01, CR02, and temperature drop percentage of CR01 on throughput of the integrated purification step. Labelled lines represent contours of constant throughput [kg/min].

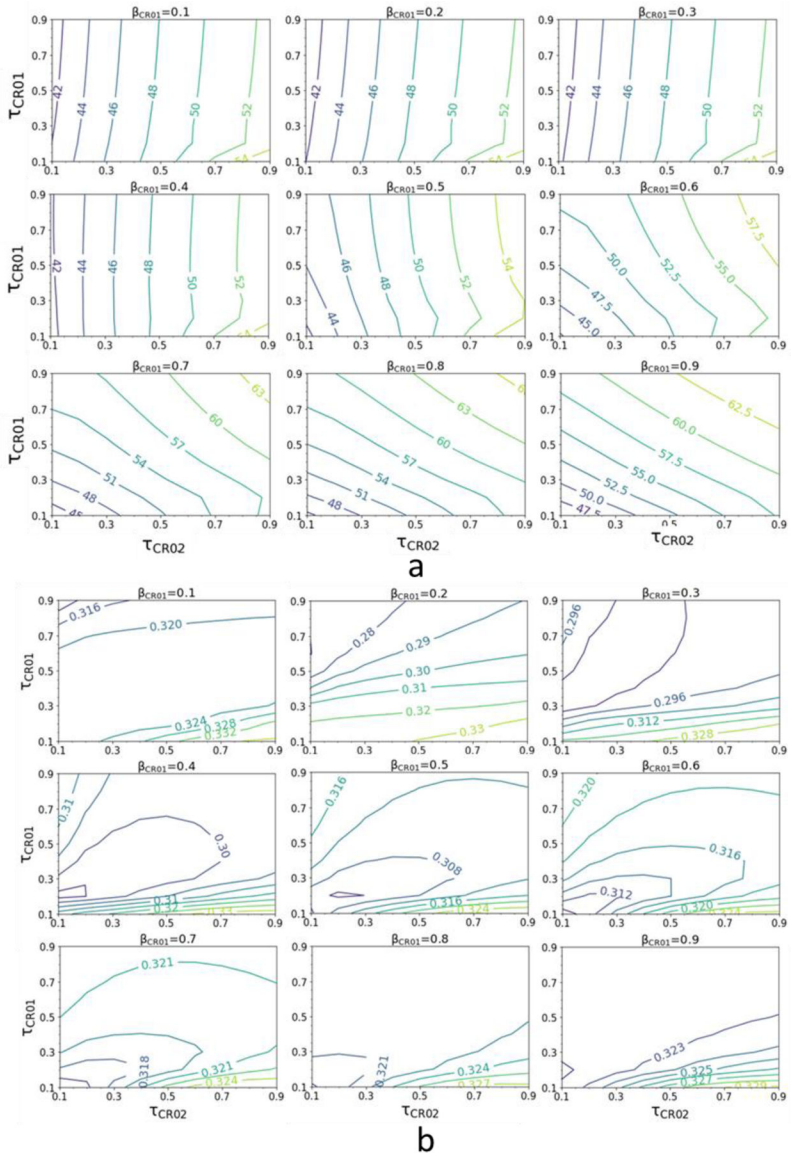

Figure 6.

(a) Effect of residence time of CR01, CR02, and temperature drop percentage of CR01 on throughput of the integrated purification step. Labelled lines represent contours of constant throughput [kg/min]; (b) Effect of residence time of CR01, CR02, and temperature drop percentage of CR01 on cake porosity. Labelled lines represent contours of constant porosity.

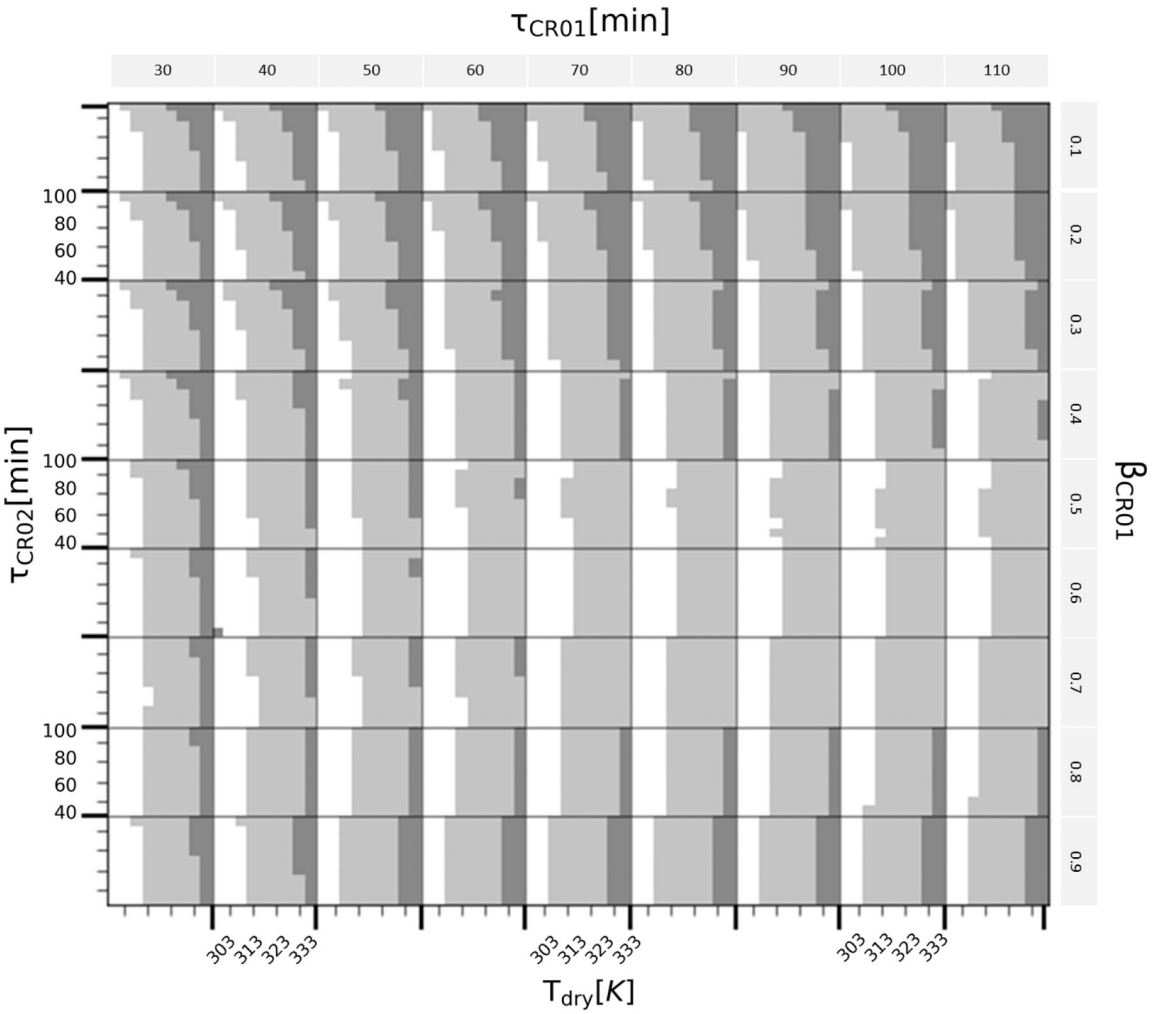

Figure 7.

Effect of residence time of CR01, CR02, temperature drop percentage of CR01, and drying gas temperature on final moisture content of the dry product. The darkest shade shows the operating condition leading to final saturation value under 7%, grey shade is when saturation is 7–15%, and white area is above 15%.

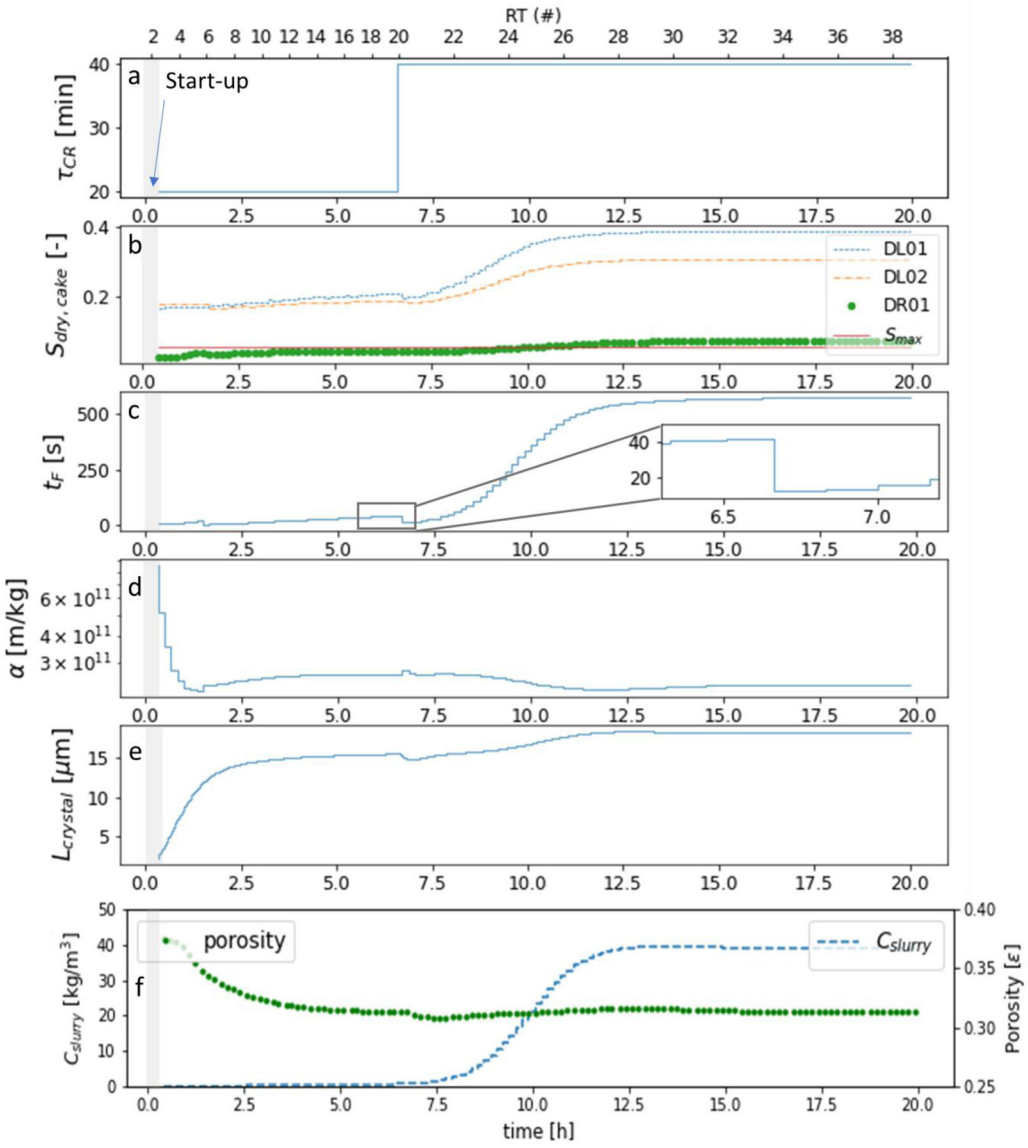

Figure 8.

Dynamic simulation result indicating process and product parameters of the integrated purification step: a) residence time (in both CR01 and CR02), b) cake saturation ($S_{dry,cake}$) after first deliquoring (DL01), second deliquoring (DL02), drying step (DR01) and maximum target saturation (S_{max}), c) filtration time estimated for the cakes for filtration step (F01), d) cake resistivity of the filter cake, e) mean crystal size produced from the crystallization step, e) concentration of slurries and porosity of the filter cake. Note that the initial start-up period in crystallization step is shown in grey shades.

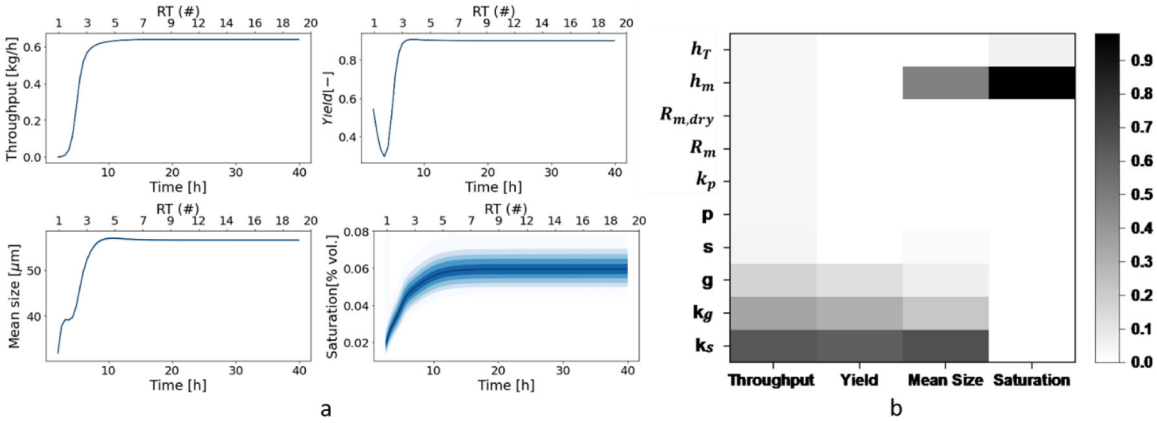

Figure 9.

(a) Dynamic response of the model outputs of uncertain model parameters; (b) Heat map for total sensitivity indices of model parameters on model outputs

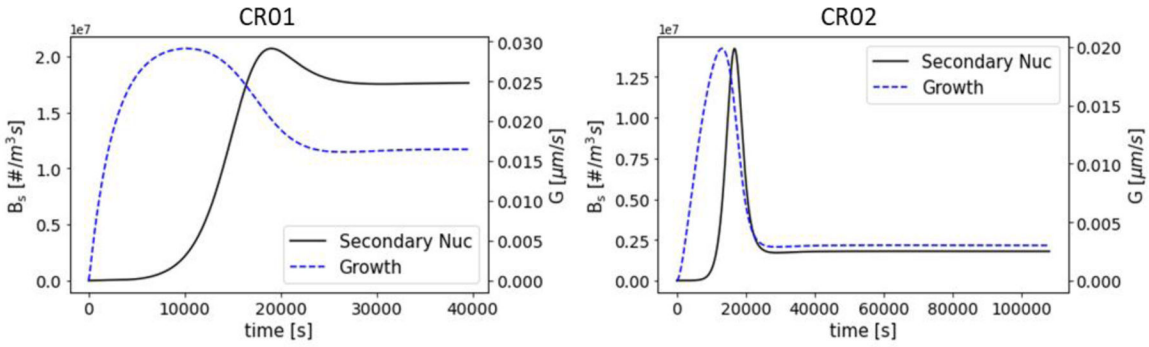

Figure 10.
Comparison of secondary nucleation and growth kinetics during crystallization step

Table 1.

Constants for the system equations

Notation	Unit of measure	Value
k_v	Volumetric shape factor	1
k_A	Surface shape factor	6
a_1	Solubility constant	−51.119
a_2	Solubility constant	950.172
a_3	Solubility constant	9.201

Table 2.

Decision variables for the flowsheet

Stage	UO	Decision variable	Measure
Crystallizer	CR01	T_{CR01} [°C]	Cooling jacket temperature of CR01
	CR01	τ_{CR01} [min]	Residence time of CR01
	CR02	τ_{CR02} [min]	Residence time of CR02
CFC	F, DL, W, DR	ΔP [Pa]	Pressure gradient
	F, DL	t_{filt}[s]	Filtration cycle time
	DR	t_{drying}[s]	Drying cycle time
	W	W [-]	Washing ratio
	DR	T_{drying} [°C]	Drying inlet gas temperature

Table 3.

Uncertain parameters for sensitivity analysis

Notation	Definition	Distribution	Nominal	Range	Units
k_p	Primary nucleation rate constant × 10^{-5}	Uniform	3.7	/3.67, 3.74/	[# $/m^3 s$]
p	Primary nucleation exponent	Uniform	2.041	/2.040, 2.042/	[−]
k_s	secondary nucleation rate constant × 10^{-4}	Uniform	7.61	/7.55, 7.70/	[# $/m^3 s$]
s	secondary nucleation exponent	Uniform	1.753	/1.752, 1.754/	[−]
k_g	growth rate constant × 10^{-4}	Uniform	2.95	/2.94, 2.96/	[m/s]
g	Growth rate exponent	Uniform	0.963	/0.962, 0.964	[−]
R_m	Filter medium resistance × 10^9	Uniform	1	/0.9, 1.1/	[$1/m$]
$R_{m,\,dry}$	Dryer filter medium resistance × 10^9	Uniform	2.22	/1.998, 2.442/	[$1/m$]
h_m	Mass transfer coefficient× 10^{-2}	Uniform	1	/0.8, 1.2/	[$mol/\mathrm{m}^2 s$]
h_T	Heat transfer coefficient	Uniform	10	/8, 12/	[$W/m^2 K$]

Table 4.

Carousel operation variables for the simulation

Decision variable	Base Case
t_{filt} [s]	175
t_{drying}[s]	175
ΔP [Pa]	3×10^5
W [-]	3
T_{drying} [°C]	50

Table 5.

Comparison between optimal solutions of the digital design of the integrated continuous purification process using two different optimization approaches.

Variables	Base Case	Optimal Case (Nelder-Mead)	Optimal Case (Genetic Algorithm)
β_{CR01} [°C/°C]	0.72	1	1
τ_{CR01} [min]	109.7833	43.6	44.0
τ_{CR02} [min]	119.46	120	120
t_{filt} [s]	102.5	50.5	51.3
t_{drying}[s]	111.4	154.75	155.05
ΔP [Pa]	3.13×10^5	5.0×10^5	4.99×10^5
W [-]	3.5	3.896	2.51
T_{drying} [°C]	52.05	70	70

Table 6.

Values of the objective function (throughput) and inequality constraints (CQAs) for the optimized purification process compared to the initial base case.

	Base Case	Optimal Case (Nelder-Mead)	Optimal Case (GA)
Throughput [kg/h]	0.19	0.676	0.638
Yield [-]	86.62	89.99	90.19
Crystal Size [μm]	64.02	57.166	56.726
Saturation [-]	0.147	0.05017	0.049
Slurry Volume [mL]	3.89	4.77	4.86

Table 7.

Total sensitivity index and ranking of the parameters on model outputs

Throughput			Yield		
Rank	**Parameter**	S_{Ti}	**Rank**	**Parameter**	S_{Ti}
1	k_s	0.6384	1	k_s	0.6133
2	k_g	0.3448	2	k_g	0.3046
3	g	0.1667	3	g	0.123
4	s	0.0448	4	s	0.0073
5	p	0.03758	5	p	0.0019978
6	k_p	0.03757	6	k_p	0.0019975
7	R_m	0.03751	7	R_m	0.0019973
	$R_{m,\,dry}$	0.03751		$R_{m,\,dry}$	0.0019973
	h_m	0.03751		h_m	0.0019973
	h_T	0.03751		h_T	0.0019973
Mean Size			**Saturation**		
Rank	**Parameter**	S_{Ti}	**Rank**	**Parameter**	S_{Ti}
1	k_s	0.6662	1	h_m	0.977313
2	k_g	0.2186	2	h_T	0.05314
3	g	0.06454	3	R_m	0.00047
4	s	0.02308	4	$R_{m,\,dry}$	0.00043
5	k_p	0.002090	5	k_s	0.000325
6	p	0.002076	6	k_g	0.000128
	R_m	0.002076	7	g	6.2e-5
	$R_{m,\,dry}$	0.002076	8	k_p	6.16e-5
	h_m	0.002076	9	s	5.98e-5
	h_T	0.002076	10	p	5.95e-5